nature aging

Article

https://doi.org/10.1038/s43587-023-00453-7

Cxxc finger protein 1 maintains homeostasis and function of intestinal group 3 innate lymphoid cells with aging

Received: 25 July 2022

Accepted: 9 June 2023

Published online: 10 July 2023

Check for updates

Xin Shen[1,2,3,4,13], Xianzhi Gao[1,3,4,5,6,13], Yikai Luo[7,8,13], Qianying Xu[3], Ying Fan[9], Shenghui Hong[9], Zhengwei Huang[3], Xiaoqian Liu[1,3], Qianqian Wang[9], Zuojia Chen[10], Di Wang[3], Linrong Lu[3], Chuan Wu[10] ✉, Han Liang[7,8,11] ✉ & Lie Wang[1,3,4,5,9,12] ✉

Aging is accompanied by homeostatic and functional dysregulation of multiple immune cell subsets. Group 3 innate lymphoid cells (ILC3s) constitute a heterogeneous cell population that plays pivotal roles in intestinal immunity. In this study, we found that ILC3s in aged mice exhibited dysregulated homeostasis and function, leading to bacterial and fungal infection susceptibility. Moreover, our data revealed that the enrichment of the H3K4me3 modification in effector genes of aged gut CCR6$^+$ ILC3s was specifically decreased compared to young mice counterparts. Disruption of Cxxc finger protein 1 (Cxxc1) activity, a key subunit of H3K4 methyltransferase, in ILC3s led to similar aging-related phenotypes. An integrated analysis revealed Kruppel-like factor 4 (Klf4) as a potential Cxxc1 target. Klf4 overexpression partially restored the differentiation and functional defects seen in both aged and Cxxc1-deficient intestinal CCR6$^+$ ILC3s. Therefore, these data suggest that targeting intestinal ILC3s may provide strategies to protect against age-related infections.

The functional deterioration of systemic immunity with aging is termed immune-senescence, which ultimately leads to poor vaccination responses, persistent low-grade inflammation and increased infection susceptibility[1–3].

T lymphocytes enter a stage of terminal differentiation with aging, resulting in a biased lineage differentiation and, therefore, a lack of plasticity, which, in turn, impairs the capacity of cells to combat neoantigens[4]. Additionally, a reduction in T cell receptor (TCR) diversity and expansion of memory over naive T cells may lead to the accumulation of senescent T cells, which are in a pro-inflammatory state that sustains inflammation[1,5]. Peripheral B cells produce excessive tumor necrosis factor (TNF) during aging, increasing the potential to affect both the regeneration of B lymphocytes and humoral immune responses[6]. Regarding innate immunity, aging not only alters the

[1]Institute of Immunology and Bone Marrow Transplantation Center, First Affiliated Hospital, Zhejiang University School of Medicine, Hangzhou, China. [2]Co-Facility Center, Zhejiang University School of Medicine, Hangzhou, China. [3]Zhejiang University School of Medicine, Hangzhou, China. [4]Liangzhu Laboratory, Zhejiang University Medical Center, Hangzhou, China. [5]Zhejiang University-University of Edinburgh Institute, Zhejiang University School of Medicine, Hangzhou, China. [6]Edinburgh Medical School: Biomedical Sciences, College of Medicine and Veterinary Medicine, University of Edinburgh, Edinburgh, UK. [7]Department of Bioinformatics and Computational Biology, The University of Texas MD Anderson Cancer Center, Houston, TX, USA. [8]Program of Quantitative and Computational Biosciences, Baylor College of Medicine, Houston, TX, USA. [9]Laboratory Animal Center, Zhejiang University, Hangzhou, China. [10]Experimental Immunology Branch, National Cancer Institute, National Institutes of Health, Bethesda, MD, USA. [11]Department of Systems Biology, The University of Texas MD Anderson Cancer Center, Houston, TX, USA. [12]Future Health Laboratory, Innovation Center of Yangtze River Delta, Zhejiang University, Jiaxing, China. [13]These authors contributed equally: Xin Shen, Xianzhi Gao, Yikai Luo. ✉e-mail: chuan.wu@nih.gov; hliang1@mdanderson.org; wanglie@zju.edu.cn

relative abundance of natural killer cells, macrophages, neutrophils and dendritic cells but also affects their respective functions (for example, cytotoxicity, phagocytosis and antigen presentation abilities)[1,7,8]. Recently, the accumulation of group 2 innate lymphoid cells (ILC2s) in the choroid plexus has been discovered in aged mice and humans, and the activation of ILC2s has been shown to alleviate aging-associated cognitive decline[9].

As a complex organ system with multiple immune cell types, the intestine shows homeostatic and functional decline with aging, but the underlying mechanisms are still incompletely understood. Retinoic acid receptor–related orphan receptor γt (RORγt)-expressing group 3 ILCs (ILC3s) localize predominantly to the intestinal lamina propria[10]. ILC3s can be primarily classified into three heterogeneous categories based on the expression of the chemokine receptor CCR6 and natural cytotoxicity-triggering receptor (NCR), including CCR6$^+$ lymphoid tissue inducer (LTi)-like ILC3s, NKp46$^+$ ILC3s and CCR6$^-$ NKp46$^-$ double-negative (DN) ILC3s[11–13]. Moreover, LTi cells persist after birth and play an essential role in promoting secondary lymphoid tissue organogenesis, such as cryptopatches and isolated lymphoid follicles[14,15]. A proportion of CCR6$^+$ ILC3s can also express CD4, and these cells are considered to be more stable than CCR6$^+$CD4$^-$ ILC3s[16,17]. Moreover, CCR6$^-$CD4$^-$ ILC3s can undergo diversification to yield terminally differentiated NKp46$^+$ ILC3s[18]. Intestinal ILC3s are essential for protection against commensal microbiota and maintaining the epithelial barrier integrity, largely because they produce IL-22 and IL-17A[10,19,20].

Epigenetic regulation, a hallmark of aging, is a vital mechanism underlying the deteriorated cellular functions observed during aging and in aging-associated diseases[21,22]. DNA methylation presents clear age-related reorganization in human classical monocytes, which have the potential to alter the antigen-presenting function of these cells[23], and its pattern changes in naive CD4$^+$ T cells with aging may be a reasonable explanation for increased autoimmunity[24]. Increasing experimental evidence indicates that aging is accompanied by changes in histone acetylation and methylation states, such as global increases in histone H4K16 acetylation and H4K20 trimethylation, whereas H3K9 methylation and H3K27 trimethylation are decreased during aging[22,25]. Moreover, trimethylation of lysine 4 on histone H3 (H3K4me3) is closely related to aging[26,27]. Aged murine hematopoietic stem cells (HSCs) display broader H3K4me3 peaks across HSC identities and stem cell self-renewal, which induces HSC dysfunction[28].

CXXC finger protein 1 (Cfp1, encoded by the *Cxxc1* gene) is a conserved subunit of the SET1 H3K4 methyltransferase, which, in complex with Setd1b, binds to DNA via its CXXC finger domain and recruits Setd1 to most CpG islands (CGIs) through its SID domain[29,30]. Recent studies showed that a lack of Cxxc1 led to impaired oocyte and thymic T cell development[31–33]. Other notable roles played by Cxxc1 include efficient murine hematopoiesis[34], Th17 cell differentiation[35] and GM-CSF-derived macrophage phagocytic and bactericidal activity[36]. The altered expression of *Cxxc1* and its reduced protein level in ovarian cells may adversely influence oocyte quality, which has been linked with female fertility loss in advancing maternal age[37].

In this study, we found that aged mice exhibited impaired homeostasis in intestinal ILC3s, which was characterized by aberrant ILC3 cell subset proportions and functions, leading to increased susceptibility to bacterial and fungal infection. Moreover, effector genes of aged gut CCR6$^+$ ILC3 displayed decreased H3K4 trimethylation compared to that of young mice. To confirm these observations, the deletion of Cxxc1 in ILC3s caused aging similar phenotypic changes, including a reduction in CCR6$^+$ ILC3s, especially the CD4$^+$ cell subset, as well as their attenuated ability to secrete IL-22 and IL-17A. An integrated analysis of single-cell RNA sequencing (scRNA-seq) revealed an analogous transcriptional landscape of ILC3s in Cxxc1-deficient and aged mice. Moreover, Kruppel-like factor 4 (Klf4), a direct target of Cxxc1, partially restored the differentiation and functional defects seen both in aged intestinal and Cxxc1-deficient CCR6$^+$ ILC3s.

Results

Homeostasis of ILC3s is dysregulated in the intestine of aged mice

We first compared the number of ILC3s in the small intestine lamina propria (siLP) of young (6–8 weeks old) and aged (18 months old) mice. We observed that male aged mice exhibited markedly elevated proportion and numbers of ILC3s and a longer small intestine (Extended Data Fig. 1a–c). When analyzing the subsets of ILC3s, we found reductions in the proportion and total numbers of CCR6$^+$ ILC3s in the Lin$^-$RORγt$^+$ ILC3 population and an increase in NKp46$^+$ ILC3s compared to the number in the control group (Fig. 1a,b). Moreover, the proportion of both CD4$^-$ and CD4$^+$ cell subsets in the CCR6$^+$ ILC3s was reduced, with the latter showing a more profound reduction. In addition, the number of DN ILC3s increased nearly two-fold in aged mice, although the percentage of these cells remained constant. To rule out the influence of sex, we analyzed the phenotype of the ILC3s in female aged mice and found results similar to those of the male (Extended Data Fig. 2a–d). In addition, the number and size of the Peyer's patches (PPs) in the small intestine were indistinguishable from those in young mice (Extended Data Fig. 1d,e).

Next, we intended to determine whether the homeostasis of aged intestinal ILC3 subsets was due to an intrinsic cellular mechanism. CD45.2$^+$ bone marrow cells from either young or aged mice were mixed with CD45.1$^+$ wild-type bone marrow cells at a 1:1 ratio and injected into sublethally irradiated recipient mice carrying CD45.1$^+$ cells. Gut lamina propria lymphocytes (LPLs) were isolated 8 weeks later, and analysis revealed no evident difference in total ILC3s of bone marrow chimeras (Extended Data Fig. 1f,g). A decrease in the number of CCR6$^+$ ILC3s of chimeric mice that received aged bone marrow cells, especially CCR6$^+$CD4$^+$ ILC3s, was observed, verifying that the maintenance of CCR6$^+$ ILC3s was endogenously regulated by aging (Fig. 1c–f). In contrast to the aforementioned findings, NKp46$^+$ and DN ILC3s from aged donor cells were not increased. Previous studies showed that the CCR6$^-$ ILC3 subset exhibited phenotypic and functional plasticity[13]. DN ILC3s are potential precursors of NKp46$^+$ ILC3s and express NKp46 and IFN-γ in a reversible process that is regulated by T-bet[12,18]. Notch can regulate the NKp46$^+$ ILC3 phenotype transition, whereas transforming growth factor-β (TGF-β) is an inhibitor[38,39]. CCR6$^+$ ILC3s were found to be relatively stable and exhibited notable differences in chromatin accessibility as well as different transcriptional levels[16,40]. The reduction in CCR6$^+$ ILC3s in aged mice more likely involves molecular regulation than environmental factors.

ILC3 function declines with age, leading to susceptibility to microbes

We wondered whether the observed changes in aged intestinal ILC3s were related to functional changes. IL-22-producing ILC3s play crucial roles in tissue homeostasis and host defense against microbes by regulating gut epithelial barrier functions[41–43]. *Citrobacter rodentium* infection has been proven to be a valid model to study intestinal inflammation[44,45]. After infection with *C. rodentium*, aged mice exhibited obviously shorter colon lengths (Fig. 2a,b), increased the number of *C. rodentium* colony-forming units (CFUs) in feces (Fig. 2c) and rapidly lost body weight compared to the young controls (Fig. 2d). The histological data demonstrated that aged mice presented clear epithelial injury, obvious crypt hyperplasia and increased infiltration of inflammatory cells (Fig. 2e). In accordance with these pathological manifestations, IL-22$^+$CCR6$^+$ ILC3s were four-fold more abundant in young mice than in aged mice, and a two-fold decrease in IL-22-producing DN ILC3s was identified (Fig. 2f,g). In comparison, the percentage of IL-22$^+$NKp46$^+$ ILC3s in the aged gut remained the same. However, we observed an obvious decline in IL-22 expression in all populations (Fig. 2h). We next examined whether ectopic expression of IL-22 could rescue aged mice from infection. We infected both young and aged mice with *C. rodentium* and administered a plasmid expressing IL-22 or a control empty

https://doi.org/10.1038/s43587-023-00453-7

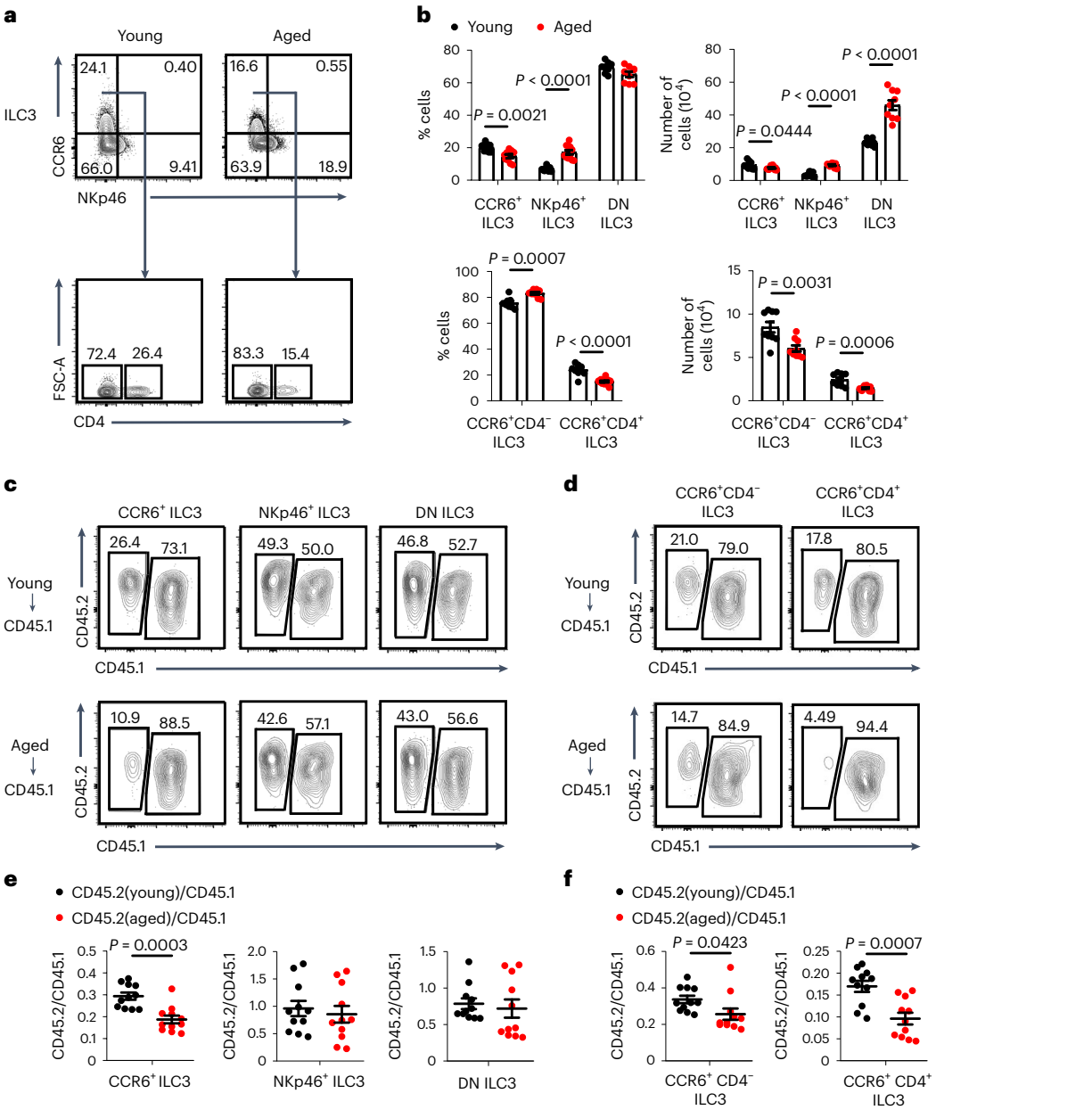

Fig. 1 | Intestinal CCR6⁺ ILC3s are numerically compromised with aging. **a**, Flow cytometry of ILC3 subsets isolated from the siLP of young (6–8 weeks old, male) and aged (18 months old, male) mice. ILC3 subsets were gated as Lin⁻RORγt⁺ and then CCR6⁺NKp46⁻, CCR6⁻NKp46⁺ or CCR6⁻NKp46⁻ (upper). The CD4⁺ ILC3 subset among the CCR6⁺ ILC3s was analyzed (below). The lineage cocktail included TCRγδ, CD3ε, CD19, CD5, Gr-1 and Ter119. **b**, The percentages and total cell numbers of three subsets were compared ($n = 8$ or 9 young, $n = 9$ or 11 aged). The percentages and total cell numbers of two subsets within CCR6⁺ ILC3s were compared ($n = 8$ or 9 young, $n = 9$ or 11 aged). **c**–**f**, Bone marrow chimeras. **c**, The expression of CD45.1 and CD45.2 in CCR6⁺ ILC3s (left), NKp46⁺ ILC3s (middle) and DN ILC3s (right) isolated from the siLP of reconstituted mice. **d**, The expression of CD45.1 and CD45.2 showing CCR6⁺CD4⁻ ILC3s (left) and CCR6⁺CD4⁺ ILC3s (right). **e**, The percentages of donor-derived cells shown in **c** (CD45.2/CD45.1) were compared ($n = 11$). **f**, The percentages of donor-derived cells shown in **d** (CD45.2/CD45.1) were compared ($n = 11$). Bar graphs are presented as mean ± s.e.m. A two-tailed Student's *t*-test was performed for comparisons. The data are representative of at least three independent experiments (**a**–**f**). FSC-A, forward scatter-area.

plasmid to them by hydrodynamic injection. We demonstrated that the increased pathology of aged mice in *C. rodentium* infection could be rescued with exogenous IL-22, as manifested by longer colon lengths, a lower fungal burden in feces, slower body weight loss and less severe inflammation and colon pathology compared to control mice without IL-22 administration (Extended Data Fig. 3a–e).

ILC3s were previously found to be essential for IL-17-dependent protection against *Candida albicans*[46]. Therefore, we infected young and aged mice with *C. albicans* by gavage. After inoculation, the aged mice developed more severe intestinal inflammation, as manifested by shorter colon lengths, a higher fungal burden in feces and more severe weight loss than colon pathology (Extended Data Fig. 4a–e). Seven days after inoculation, fewer IL-17A⁺ ILC3s were present in the small intestines of the aged mice compared to the young controls (Extended Data Fig. 4f,g). In addition, we tested IFN-γ secretion levels in aged gut NKp46⁺ ILC3s and found that they remained roughly unchanged after ex vivo stimulation (Extended Data Fig. 4h).

However, efficient control of pathogenic microbial infection in mice requires synergy between the innate and adaptive immune systems[45]. To rule out the effects of the acquired immune system in vivo,

https://doi.org/10.1038/s43587-023-00453-7

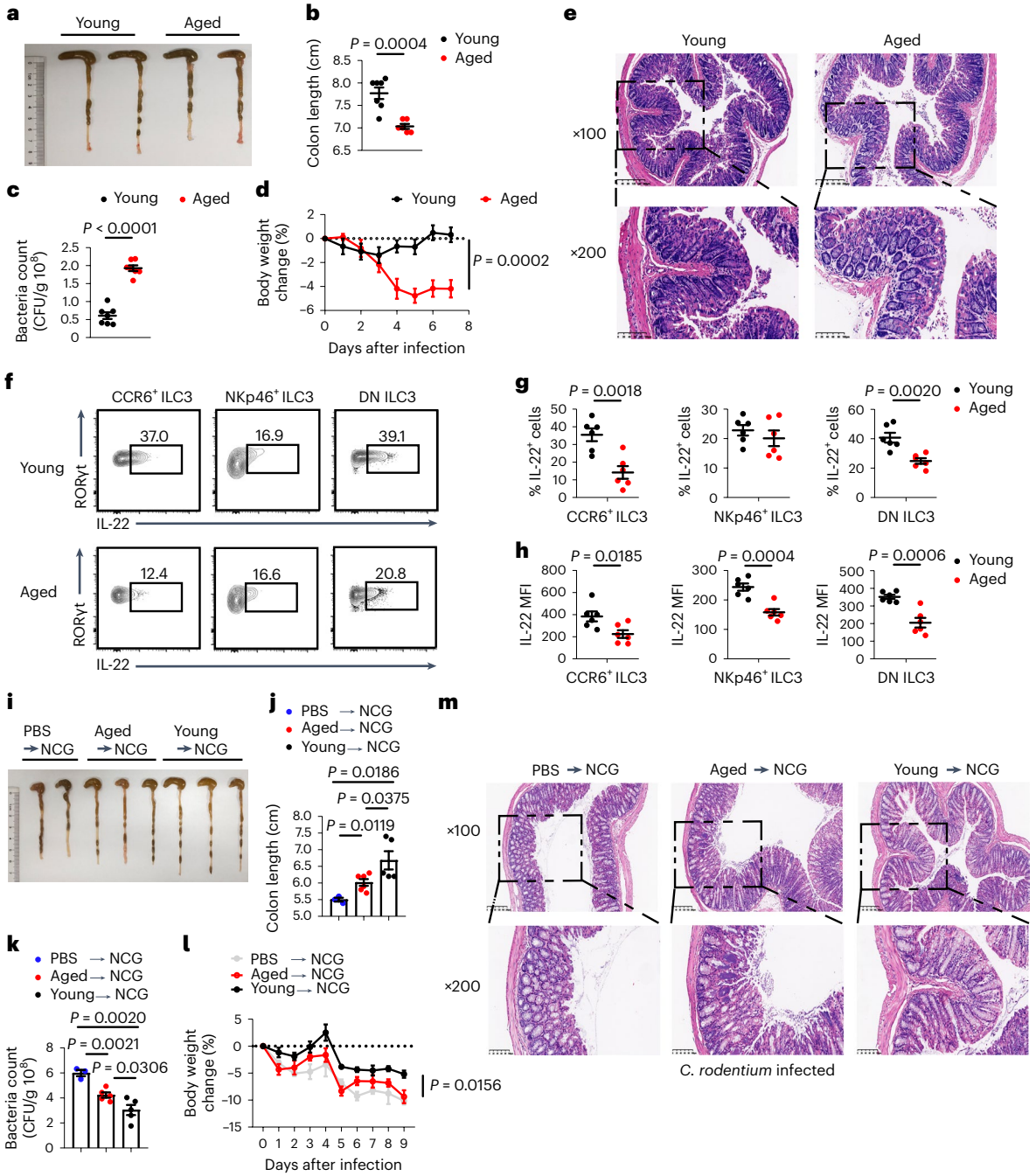

Fig. 2 | Defective ILC3 function in aged mice compromises host defense against *C. rodentium* infection. a–**h**, *C. rodentium* infection model. **a**, Representative colon lengths of young and aged mice after oral inoculation with *C. rodentium* on day 7. **b**, Summary of colon lengths in infected mice ($n = 7$ young, $n = 6$ aged). **c**, *C. rodentium* CFUs in feces 7 d after infection ($n = 7$). **d**, Body weight changes of young and aged mice after infection at the indicated timepoints ($n = 9$). **e**, Representative images (×100 and ×200) of colons from infected mice stained with H&E. **f**, Flow cytometric analysis of IL-22 expression in CCR6$^+$ ILC3s (left), NKp46$^+$ ILC3s (middle) and DN ILC3s (right) isolated from the siLP 7 d after infection. **g**, The percentages of IL-22$^+$ cells in the indicated cell populations were compared ($n = 6$). **h**, Mean fluorescence intensity (MFI) of IL-22 in the indicated cells ($n = 6$). **i**–**m**, ILC3s (Lin$^-$CD127$^+$CD27$^-$KLRG1$^-$) from young and aged mice were adoptively transferred into NCG mice with *C. rodentium* infection. **i**,**j**, Measurements and statistical analysis of the colon lengths from NCG recipients ($n = 3$ control, $n = 5$ young transferred, $n = 6$ aged transferred). **k**, CFUs in the feces of NCG recipients 9 d after infection ($n = 3$ control, $n = 5$ transferred group). **l**, Changes in body weight were recorded at the indicated timepoints ($n = 3$ control, $n = 5$ transferred group). **m**, Histological analysis of colonic tissues by H&E staining. Bar graphs are presented as mean ± s.e.m. A two-tailed Student's *t*-test was performed for comparisons. The data are representative of three (**a**–**h**) and two (**i**–**m**) independent experiments.

we performed adoptive transfer of gut ILC3s purified from either young or aged mice into NCG mice, in which neither ILCs nor T/B cells are produced. Control NCG mice were injected with an equal volume of PBS. Twenty-four hours after adoptive transfer, recipient NCG mice were orally inoculated with *C. rodentium*. Nine days later, the colon length of the mice injected with aged intestinal ILC3s was found to be shorter than that of the mice receiving young intestinal cells but longer than that of the mice that received PBS (Fig. 2i,j). ILC3s derived from aged mice lost their protective capability, manifested by increased CFUs (Fig. 2k), faster weight loss and more severe intestinal injury

than young intestinal ILC3s (Fig. 2l,m). Similar results were observed in NCG mice infected with *C. albicans*, and mice receiving aged intestinal ILC3s exhibited more severe inflammation (Extended Data Fig. 4i–m). In conclusion, the exacerbation of pathogenic microbial infection in aged mice was mediated in a cell-intrinsic manner.

ILC3 effector genes are modified with decreased H3K4me3 during aging

To assess dynamic changes in the transcriptional levels of ILC3s during senescence, we sorted ILC3s (Lin$^-$KLRG1$^-$CD27$^-$CD127$^+$) obtained from young and aged mice and analyzed by scRNA-seq (BD Rhapsody). Low-quality and contaminating cells expressing mitochondrial transcripts were excluded from further analysis. The total number of recovered cells was 8,972, with a reasonable median gene count, 1,287. Based on the expressions of canonical ILC3 state markers, we identified all three well-established clusters, namely CCR6$^+$, NKp46$^+$ and DN, plus a fourth cluster characterized by high proliferation activity (Fig. 3a,b). The MHC-II chaperone Cd74 and the transcription factor Zfp36 are enriched in CCR6$^+$ cells. In contrast, *Ikzf3* encoding a zinc-finger protein and *Ifngr1* encoding a major interferon receptor are enriched in NKp46$^+$ cells (Fig. 3c).

We next investigated the alterations of cell lineage abundance driven by aging. In concordance with our flow cytometry data, CCR6$^+$ ILC3s were depleted in the gut of aged mice (accounting for ~20% versus ~50% of all ILC3s in young mice), whereas aged gut NKp46$^+$ cells saw an increase (accounting for ~70% compared to ~30% of all ILC3s in young mice). The abundance of DN cells or proliferative cells did not show a change during aging (Fig. 3d). These patterns were confirmed using an unbiased differential abundance testing approach, Milo, which showed a prominent concentration of aged mice gut ILC3s in the NKp46$^+$ domain and young mice gut ILC3s in the CCR6$^+$ domain (Fig. 3e).

Increasing evidence indicates that multiple histone modifications through established epigenetic mechanisms modulate the deterioration in cellular functions observed during aging[47,48]. Among these epigenetic modifications, H3K4me3 has attracted much interest because it varies in a plethora of cell types and organisms during aging. In this study, we found a downward shift of the expression levels of genes encoding H3K4 regulators (including methyltransferases, Setd1a, Mll1, Mll2 and Mll4; ref. 49) in ILC3s from young mice to aged mice (Fig. 3f). This trend is consistent across the lineages, indicating a pan-ILC3 dysfunction of H3K4me3 machinery (Fig. 3f). Moreover, Cxxc1 expression was downregulated at both the RNA and protein levels in aged intestinal ILC3s (Extended Data Fig. 5a). Therefore, we sought to determine whether the epigenetic profiles of gut ILC3s are altered during aging. We performed cleavage under targets and tagmentation (CUT&Tag) to characterize the genome-wide profiles of the H3K4me3 modification. Among the differentially H3K4me3-modified regions in aged gut CCR6$^+$ ILC3s, most of them were on the downregulated side. Compared to CCR6$^+$ ILC3s, NKp46$^+$ ILC3s or DN ILC3s showed minimal H3K4me3 alterations, suggesting that the H3K4me3 modification in CCR6$^+$ ILC3s plays a role in senescence (Fig. 3g). Moreover, effector signature genes in aged gut CCR6$^+$ ILC3s showed less H3K4me3 occupancy than those in young mice, and the modification of signature genes related to NKp46$^+$ ILC3s also decreased but to a much lesser extent (Fig. 3g,h). In aged gut CCR6$^+$ ILC3s and DN ILC3s, signature genes, such as *Ccr6*, *Cd4* and *Il17a*, exhibited a reduced activating histone methylation (H3K4me3) pattern at promoter regions compared to that in the young group, whereas no difference in H3K4me3 marks was observed in NKp46$^+$ ILC3s (Fig. 3i). In contrast, the abundance of the H3K4me3 modification in genes such as *Il22* and *Il17f* in three subsets of aged gut ILC3s was decreased. Except for the ILC marker gene, KEGG analyses of top 100 genes with down-regulated H3K4me3 modification regions in aged mice showed enrichment in signaling pathways related to aging and cancer (Extended Data Fig. 5b,c). Most of these genes showed decreased histone methylation pattern in aged gut CCR6$^+$ ILC3s when compared to NKp46$^+$ ILC3s or DN ILC3s (Extended Data Fig. 5d). In summary, our results indicated that the senescence of ILC3s was accompanied by changes in H3K4me3 abundance, and the most notable changes of H3K4me3 depositions in aged gut ILC3s preferentially occurred at genes related to CCR6$^+$ ILC3s.

Cxxc1 deletion in ILC3s leads to homeostatic dysregulation

We crossed *Cxxc1*$^{flox/flox}$ mice with *Rorc*-cre mice to delete *Cxxc1* in RORγt$^+$ ILC3s[50]. Phenotypic analysis of intestinal RORγt$^+$ ILC3s showed that the percentage and absolute number of these cells were not markedly changed in *Cxxc1*$^{f/f}$ *Rorc*^{cre} mice compared to littermate controls (Extended Data Fig. 6a,b). Similar to the phenotypes of aged mice, a two-fold reduction in the proportion and number of CCR6$^+$ ILC3s was observed in *Cxxc1*$^{f/f}$ *Rorc*^{cre} mice, although NKp46$^+$ ILC3s remained largely unchanged. Moreover, the percentage of DN ILC3s increased, and the total number remained stable. Among CCR6$^+$ ILC3s, the reduction in CCR6$^+$CD4$^+$ ILC3s was more pronounced than that in CCR6$^+$CD4$^-$ ILC3s (Fig. 4a,b). ILC3s are derived from common lymphoid progenitors (CLPs), which arise from fetal liver or bone marrow HSCs, and sequentially progress through αLP/CHILP/ILCP stages[51–53]. We observed that the frequencies and absolute numbers of CLPs, αLPs, CHILPs and ILCPs from the *Cxxc1*$^{f/f}$ *Rorc*^{cre} mice were identical to those in their littermate control mice (Extended Data Fig. 6c,d). Additionally, Cxxc1-deficient mice exhibited normal PP distribution, and PPs were similar, both in number and size, to those in wild-type mice (Extended Data Fig. 6e–g).

Next, mixed bone marrow chimeras of CD45.2$^+$ *Cxxc1*$^{f/f}$ or *Cxxc1*$^{f/f}$ *Rorc*^{cre} with CD45.1$^+$ wild-type bone marrow cells illustrated a cell-intrinsic role for Cxxc1 in regulating CCR6$^+$ ILC3 homeostasis (Fig. 4c–f). The small intestinal lamina propria reconstituted with *Cxxc1*$^{f/f}$ *Rorc*^{cre} bone marrow contained a lower percentage of CCR6$^+$ ILC3s than that in mice transplanted with *Cxxc1*$^{f/f}$ bone marrow. Although the percentage of CCR6$^+$CD4$^-$ ILC3s was reduced, that of CCR6$^+$CD4$^+$ ILC3s was almost absent in *Cxxc1*$^{f/f}$ *Rorc*^{cre} bone marrow chimeras. Similarly, no apparent alterations in NKp46$^+$ ILC3 or DN ILC3 numbers were observed in *Cxxc1*$^{f/f}$ *Rorc*^{cre} chimeras. Taken together, these data indicate that Cxxc1 deletion in ILC3s led to dysregulated homeostasis similar to that in aged mice.

Fig. 3 | Transcriptome profile of ILC3s from young and aged mice at the single-cell level. a,**b**, UMAP plots visualizing cell state annotations (**a**) and marker gene expressions (**b**) in ILC3 cells from young and aged mice. **c**, Bubble plot showing the expressions of marker genes across cell states with the dot size indicating the percentage of marker-positive cells and the color indicating average expression level. **d**, Box plots displaying the differences in each of the four cell state fractions between young and aged mice ($n = 2$). The middle line in the box is the mean; the bottom and top of the box are the first and third quartiles; and the whiskers extend to the 1.5× interquartile range of the lower and the upper quartiles, respectively. Two-sided Student's *t*-test was used to calculate the *P* values. **e**, UMAP plots showing Milo differential abundance testing results. Nodes are neighborhoods, colored by their log fold change between aged (right) and young (left) mice. Node sizes correspond to the number of cells in each neighborhood. **f**, Bubble plots depicting the expressions of H3K4me3-related epigenetic regulators in CCR6$^+$ (left), NKp46$^+$ (middle) and DN (right) ILC3s of young and aged mice. Details are the same as in **c**. **g**, Volcano plots of H3K4me3 differentially modified genes in CCR6$^+$ (left), NKp46$^+$ (middle) and DN (right) ILC3s between young and aged mice. Substantially changed genes (false discovery rate (FDR) < 0.05) and the signature genes of CCR6$^+$ and NKp46$^+$ ILC3s are highlighted. Wald test implemented in the R package DESeq2 was used to calculate the *P* values. **h**, Gene set enrichment analysis (GSEA) of CCR6$^+$ and NKp46$^+$ ILC3 signature gene sets enriched in H3K4me3-hypo-modified genes in the CCR6$^+$ and NKp46$^+$ ILC3s of aged mice, respectively. **i**, Genome track view of representative gene loci showing H3K4me3 peaks. FC, fold change; NES, normalized enrichment score.

https://doi.org/10.1038/s43587-023-00453-7

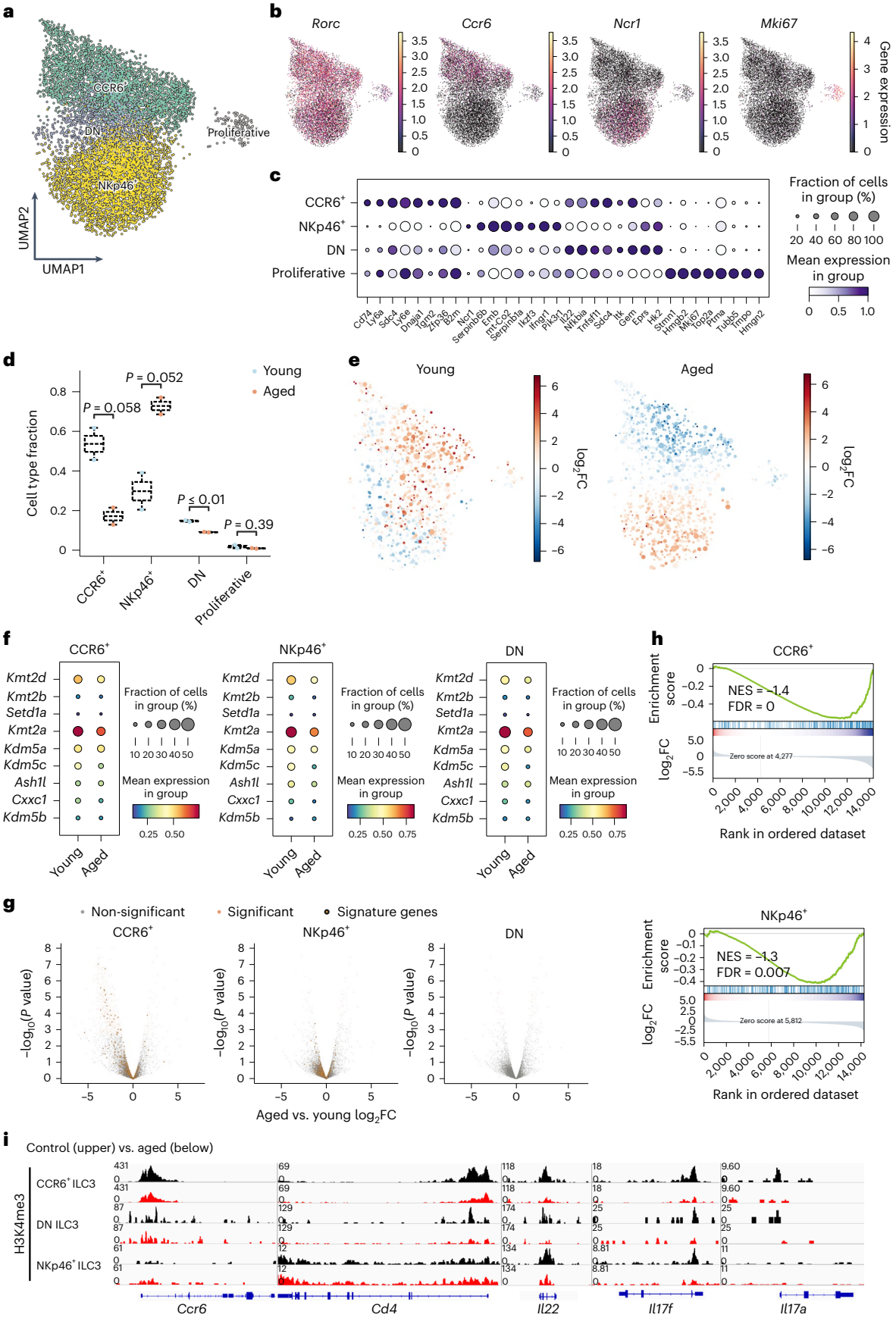

https://doi.org/10.1038/s43587-023-00453-7

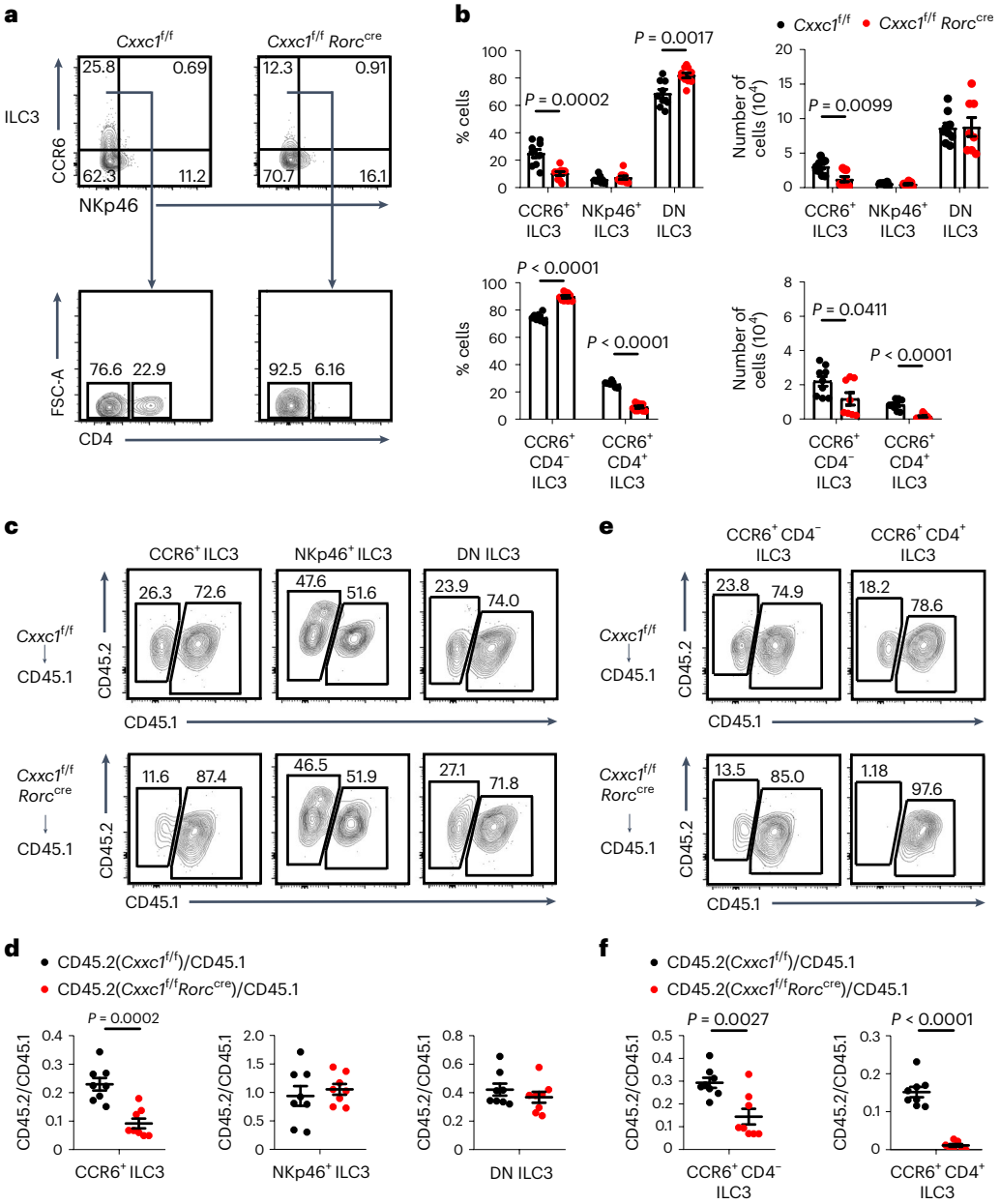

Fig. 4 | Cxxc1 is required to maintain ILC3 homeostasis. a, Flow cytometry of ILC3 subsets isolated from the siLP in *Cxxc1*$^{f/f}$ *Rorc*^{cre} (KO) mice and their *Cxxc1*$^{f/f}$ (WT) littermates. ILC3 subsets were gated as Lin$^-$RORγt$^+$ and then CCR6$^+$NKp46$^-$, CCR6$^-$NKp46$^+$ or CCR6$^-$NKp46$^-$ (upper). The CD4$^+$ ILC3 subset among the CCR6$^+$ ILC3s was analyzed (below). The lineage cocktail included TCRγδ, CD3ε, CD19, CD5, Gr-1 and Ter119. **b**, The percentages and total cell numbers of three subsets were compared ($n = 7$ or 9 WT, $n = 8$ or 10 KO). The percentages and total cell numbers of two subsets within CCR6$^+$ ILC3s were compared ($n = 7$ or 9 WT, $n = 8$ or 10 KO). **c**–**f**, Bone marrow chimeras. **c**,**e**, Flow cytometry analysis of CD45.1 and CD45.2 expression in the indicated ILC3 subsets isolated from the siLP of reconstituted mice. **d**,**f**, The percentages of donor-derived cells in the indicated ILC3 subsets (CD45.2/CD45.1) were compared ($n = 8$). Bar graphs are presented as mean ± s.e.m. A two-tailed Student's *t*-test was performed for comparisons. The data are representative of three independent experiments (**a**–**f**). KO, knockout; WT, wild-type.

Cxxc1-deficient ILC3s show defective cytokine profile

We next evaluated effector cytokine expression in Cxxc1-deficient ILC3s. Compared to control mice, *Cxxc1*$^{f/f}$ *Rorc*^{cre} mice exhibited an attenuated ability to control *C. rodentium* infection, as characterized by shortening of the colon (Fig. 5a,b). Knockout mice harbored a higher bacterial level in their feces (Fig. 5c) and did not regain their initial body weight (Fig. 5d). Furthermore, histological analysis revealed chronic infiltration of inflammatory cytokines in the *Cxxc1*$^{f/f}$ *Rorc*^{cre} mice (Fig. 5e). We also determined that, in the absence of Cxxc1, CCR6$^+$ and DN ILC3s showed reduced secretion of IL-22 (Fig. 5f,g).

We also constructed a *C. albicans* infection model in the Cxxc1-deficient mice. The pathological findings that we obtained were in line with the *C. rodentium* infection model, implying insufficient clearance of *C. albicans* (Extended Data Fig. 7a–e). All subsets of ILC3s exhibited decreased production of IL-17A in the absence of Cxxc1 except for the NKp46$^+$ ILC3s (Extended Data Fig. 7f,g). Our data suggest that ILC3s in *Cxxc1*$^{f/f}$ *Rorc*^{cre} mice failed to protect the host from fungal infection because of diminished IL-17A production. Following an unchanged NKp46$^+$ ILC3 phenotype in the absence of Cxxc1, no difference was observed in IFN-γ secretion after in vitro stimulation or *Salmonella typhimurium* infection (Extended Data Fig. 7h,i).

https://doi.org/10.1038/s43587-023-00453-7

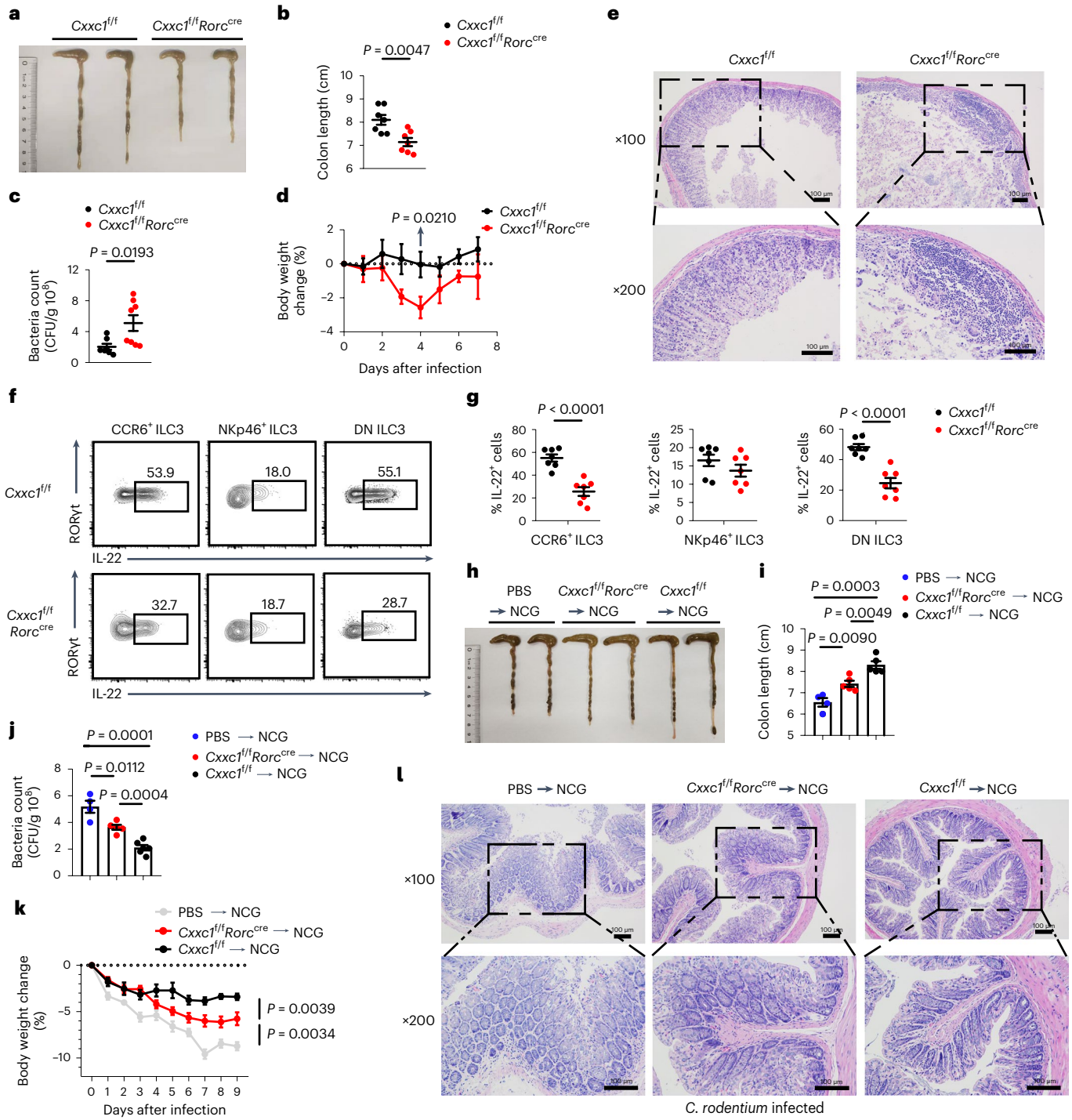

Fig. 5 | Defective ILC3 function in Cxxc1-deficient mice compromises host defense against *C. rodentium* infection. a–**g**, *C. rodentium* infection model. **a**,**b**, Colon lengths of *Cxxc1*$^{f/f}$ and *Cxxc1*$^{f/f}$ *Rorc*^{cre} mice ($n = 7$). **c**, Bacterial counts in feces ($n = 7$ WT, $n = 8$ KO). **d**, Body weight changes were monitored at the indicated timepoints ($n = 9$). **e**, H&E staining of colon tissue sections. **f**,**g**, Representative flow plots and quantification of IL-22 production by CCR6$^+$ ILC3s (left), NKp46$^+$ ILC3s (middle) and DN ILC3s (right) isolated from the siLP ($n = 7$). **h**–**l**, *Cxxc1*$^{f/f}$ or *Cxxc1*$^{f/f}$ *Rorc*^{cre} ILC3s (Lin$^-$CD127$^+$CD27$^-$KLRG1$^-$) were adoptively transferred into NCG mice with *C. rodentium* infection. **h**,**i**, Colon lengths of the NCG mouse recipients ($n = 4$ control, $n = 5$ transferred group). **j**, Bacteria counts in feces 9 d after infection ($n = 4$ control, $n = 6$ WT transferred, $n = 5$ KO transferred). **k**, Body weight changes at the indicated timepoints ($n = 7$ control, $n = 9$ WT transferred, $n = 10$ KO transferred). **l**, Representative H&E staining of colon sections. Bar graphs are presented as mean ± s.e.m. A two-tailed Student's *t*-test was performed for comparisons. The data are representative of five (**a**–**g**) and two (**h**–**l**) independent experiments. KO, knockout; WT, wild-type.

To specifically examine the effector function of ILC3s during infection, we sorted intestinal ILC3s from *Cxxc1*$^{f/f}$ or *Cxxc1*$^{f/f}$ *Rorc*^{cre} mice and adoptively transferred these cells into NCG mice and then generated a *C. rodentium* infection model. Nine days after infection, the NCG mice receiving Cxxc1-deficient ILC3s developed more severe infection than mice that received *Cxxc1*$^{f/f}$-ILC3 cells. Specifically, the colon length of the Cxxc1-deficient NCG mice was shorter (Fig. 5h,i); the *C. rodentium* colony count was higher (Fig. 5j);

https://doi.org/10.1038/s43587-023-00453-7

their body weight decreased faster (Fig. 5k); and the damage to the colon epithelial barrier was more pronounced (Fig. 5l). Additionally, NCG mice transferred with Cxxc1-deficient ILC3s displayed more severe pathological conditions when inoculated with *C. albicans*, implying a poor clearance of fungus (Extended Data Fig. 7j–n). In summary, these data suggest that the increased sensitivity to *C. rodentium* and *C. albicans* infection in Cxxc1-deficient mice occurs in a cell-intrinsic manner.

https://doi.org/10.1038/s43587-023-00453-7

Fig. 6 | Single-cell profiling reveals similarities in the transcriptional landscape between Cxxc1-deficient and aged gut ILC3s. a, UMAP plots visualizing group conditions in ILC3 cells from young, aged and *Cxxc1*$^{f/f}$ *Rorc*^{cre} mice. **b**, Stacked bar plot depicting cell state proportions across scRNA-seq samples. **c**, Box plots displaying the differences in each of the four cell state fractions between young and *Cxxc1*$^{f/f}$ *Rorc*^{cre} mice ($n = 2$). The middle line in the box is the mean; the bottom and top of the box are the first and third quartiles; and the whiskers extend to the 1.5× interquartile range of the lower and the upper quartiles, respectively. One-sided Student's *t*-test was used to calculate the *P* values. **d**, UMAP plot showing Milo differential abundance testing results. Nodes are neighborhoods, colored by their log fold change between young and *Cxxc1*$^{f/f}$ *Rorc*^{cre} mice. Node sizes correspond to the number of cells in each neighborhood. **e**, Density plots of correlations across cell states between the gene-wise $\log_2$ fold changes in the comparison of *Cxxc1*$^{f/f}$ *Rorc*^{cre} mice against young mice and those in the comparison of aged mice against young mice. Genes of substantial changes ($P < 0.05$) in both comparisons are highlighted in red. Spearman's correlation test was used to calculate the *P* values. R_s, Spearman's correlation coefficient. **f**, Bar plots showing enriched Gene Ontology (GO) biological processes for co-downregulated genes matching results of each cell state in **g**, respectively. **g**, Venn plot displaying the overlap of co-downregulated genes between cell states. **h**, Heat map visualizing the gene-wise *z*-scores of pseudo-bulk expression levels of five key immune response genes across scRNA-seq samples. Cell states and mouse conditions of each pseudo-bulk are annotated in the top panel. FC, fold change.

Similar transcriptional landscape of Cxxc1-deficient and aged ILC3s

To elucidate the mechanism by which Cxxc1 induces ILC3 lineage maintenance, we performed scRNA-seq on Cxxc1-deficient ILC3s and compared the results to those obtained from young or aged gut ILC3s (Fig. 6a). Phenocopying aging-induced suppression of CCR6$^+$ ILC3s, Cxxc1-deficient mice showed a markedly decrease in CCR6$^+$ ILC3 proportion compared with young mice, similar to the aging-induced suppression (Fig. 6b,c). Accordingly, there was an increase of NKp46-specific ILC3s and DN cells in Cxxc1-knockout mice (Fig. 6b,c). An unbiased graph-based differential abundance testing confirmed the depletion of Cxxc1-deficient gut ILC3s in the CCR6$^+$ area (Fig. 6d).

In addition to the analogous switches of ILC3 subpopulations in terms of their abundance, we also observed a strong positive correlation between the transcriptome-perturbing effect of aging and that of Cxxc1 loss of function. We performed a differential expression analysis on the pseudo-bulks of each combination of an ILC3 lineage and a mouse condition to obtain robust statistical significance based on real biological replicates. This analysis showed that gene expressions were similarly modulated by aging and by Cxxc1 knockout across lineages (Fig. 6e). When searching for biological functions characterized by these common differentially expressed genes, we noticed a convergence across subpopulations of co-downregulated genes in showing enrichment in signaling pathways related to immune activation, such as 'cellular response to cytokine stimulus', 'cytokine-mediated signaling pathway' and 'cell chemotaxis' (Fig. 6f).

A closer examination of these co-downregulated genes showed that 18 of them overlapped among the lineages and contained key effector mediators, such as *Il17f* and *Ccr1* (Fig. 6g). They demonstrated consistently diminished expressions in aged and Cxxc1-deficient ILC3s across populations and biological replicates (Fig. 6h), suggesting a common theme of ILC3s' dysfunctions being the suppression of their ability as immune activators. Together, our simultaneous single-cell profiling of young, aged and Cxxc1-deficient gut ILC3s enabled an in-depth comparative analysis that pointed to a similarity between aging and H3K4me3 inhibition when it comes to being an underlying force of ILC3 anergy.

Combined analysis identified Klf4 as a potential target of Cxxc1

We sought to determine whether the epigenetic profile was altered in Cxxc1-deficient ILC3s. Of all the ILC3 subsets, a reduction in Cxxc1 occupancy was observed within 3 kilobases (kb) of transcription start sites (TSSs) and transcription end sites (TESs) across the whole genome in ILC3s (Fig. 7a,b and Extended Data Fig. 8a,b). An analysis of genome-wide peak distribution revealed that most Cxxc1-binding sites were enriched at promoters (within 1 kb), distal intergenic regions and other introns (Extended Data Fig. 8c). Moreover, H3K4me3 enrichment at all promoters of CCR6$^+$ ILC3s and DN ILC3s was reduced, whereas it was largely unchanged in NKp46$^+$ ILC3s (Fig. 7c,d and Extended Data Fig. 8d,e). Genome-wide H3K4me3 marks were identified, with more than three-quarters of the H3K4me3 modification sites located in promoter regions (Extended Data Fig. 8f). To correlate H3K4me3 modifications with gene expression and identify the ILC3-relevant genes that may be directly regulated by Cxxc1, we examined putative Cxxc1-binding sites and compared them pairwise with those in genes that exhibited decreased H3K4me3 signal intensities among the ILC3 subsets (Fig. 7e and Extended Data Fig. 8g,h). More than half of the downregulated Cxxc1-binding peaks were associated with reduced H3K4me3 abundance in the three subsets, especially in the Cxxc1-deficient CCR6$^+$ ILC3s. Then, the compromised enrichment of Cxxc1 and H3K4 trimethylation was visualized at representative genome browser tracks of effector genes in ILC3s (Fig. 7f). We found marked Cxxc1-binding peaks on key signature genes encoding transcription factors, such as *Cxxc1*, *Klf4* and *Ahr*. Ablation of Cxxc1 in those genomes reduced H3K4me3 modification levels in Cxxc1-deficient CCR6$^+$ ILC3s and DN ILC3s (Fig. 7f). Similar Cxxc1-binding peaks were observed in effector genes such as *Il22*, *Il17a* and *Il17f*, and lower densities of H3K4me3 marks at these genes were observed in Cxxc1-deficient ILC3s. The factor Ahr, which contributed to IL-22 secretion[54], was also found to be decreased in ILC3s of both aged and Cxxc1-deficient mice (Extended Data Fig. 8i,j).

Next, we investigated the expression of Klf4 within ILC3 subsets from *Cxxc1*$^{f/f}$ and *Cxxc1*$^{f/f}$ *Rorc*^{cre} mice by capillary western immunoassay (Fig. 7g,h). The analysis showed that the expression of Klf4 was

Fig. 7 | Genome-wide chromatin sequencing and rescue experiments revealed that Klf4 is a potential target of Cxxc1 in CCR6$^+$ ILC3. a, Heat map showing the genome-wide distribution of Cxxc1-binding signals at peak centers in CCR6$^+$ ILC3s sorted from control and Cxxc1-deficient mice by CUT&Tag. **b**, Occupancy of Cxxc1 at all gene promoter regions (±3 kb of the TSS). Each line represents the average read coverage over all gene promoter regions. **c**, Heat maps illustrating enrichment of H3K4me3 CUT&Tag signals at all gene promoters (±3 kb of TSSs) in CCR6$^+$ ILC3s. **d**, Average methylation (H3K4me3) levels at the promoters (±3 kb of TSSs) of all genes in CCR6$^+$ ILC3s. **e**, Venn diagram showing genes with reduced enrichment of Cxxc1 and H3K4me3 modification (chi-squared test was used to calculate the *P* values). Adjusted absolute $\log_2$ fold change > 0.5 and adjusted $P < 0.05$. **f**, Genome track view of representative gene loci showing Cxxc1-binding (upper) and H3K4me3 (below) peaks at the indicated loci in ILC3 subsets (CCR6$^+$ ILC3s are black, DN ILC3s are blue and NKp46$^+$ ILC3s are red). **g**, Immunoblot images showing Klf4 protein in ILC3 subsets sorted from *Cxxc1*$^{f/f}$ and *Cxxc1*$^{f/f}$ *Rorc*^{cre} mice. **h**, The relative protein content was normalized to that of β-actin ($n = 3$). **i**–**l**, Rescue experiments. **i**, Flow cytometry of CD45.2$^+$GFP$^+$ ILC3 subsets isolated from the siLP in the indicated recipient mice. **j**, The percentages of the indicated subsets were compared ($n = 4$ WT+PMX, $n = 5$ or 7 KO+PMX, $n = 6$ or 7 KO+Klf4). **k**, Cytokine production in siLP CD45.2$^+$GFP$^+$ ILC3s from the indicated recipient mice. **l**, The percentages of IL-22$^+$ ILC3s were compared ($n = 6$ WT or KO+PMX, $n = 7$ KO+Klf4). The percentages of IL-17A$^+$ ILC3s were compared ($n = 6$ WT+PMX, $n = 7$ KO+PMX, $n = 6$ KO+Klf4). Bar graphs are presented as mean ± s.e.m. A two-tailed Student's *t*-test was performed for comparisons. The data are representative of at least three independent experiments (**i**–**l**). FSC-A, forward scatter-area; KO, knockout; WT, wild-type; PMX, PMX-GFP retrovirus.

https://doi.org/10.1038/s43587-023-00453-7

higher in CCR6$^+$ ILC3s and decreased in Cxxc1-deficient mice. To further explore the role played by Klf4 in Cxxc1-deficient ILC3s, we infected CLPs from *Cxxc1*$^{f/f}$*Rorc*^{cre} mice with Klf4$^-$ retroviral vectors, providing long-term modulation of *Klf4* expression in infected cells and their progeny[55]. Retrovirus-transfected CLPs were transferred into sublethally irradiated CD45.1$^+$ recipient mice that were sacrificed 2 weeks later for analysis. The results showed that the overexpression of Klf4 potently increased the percentage of CCR6$^+$ ILC3s relative to that in

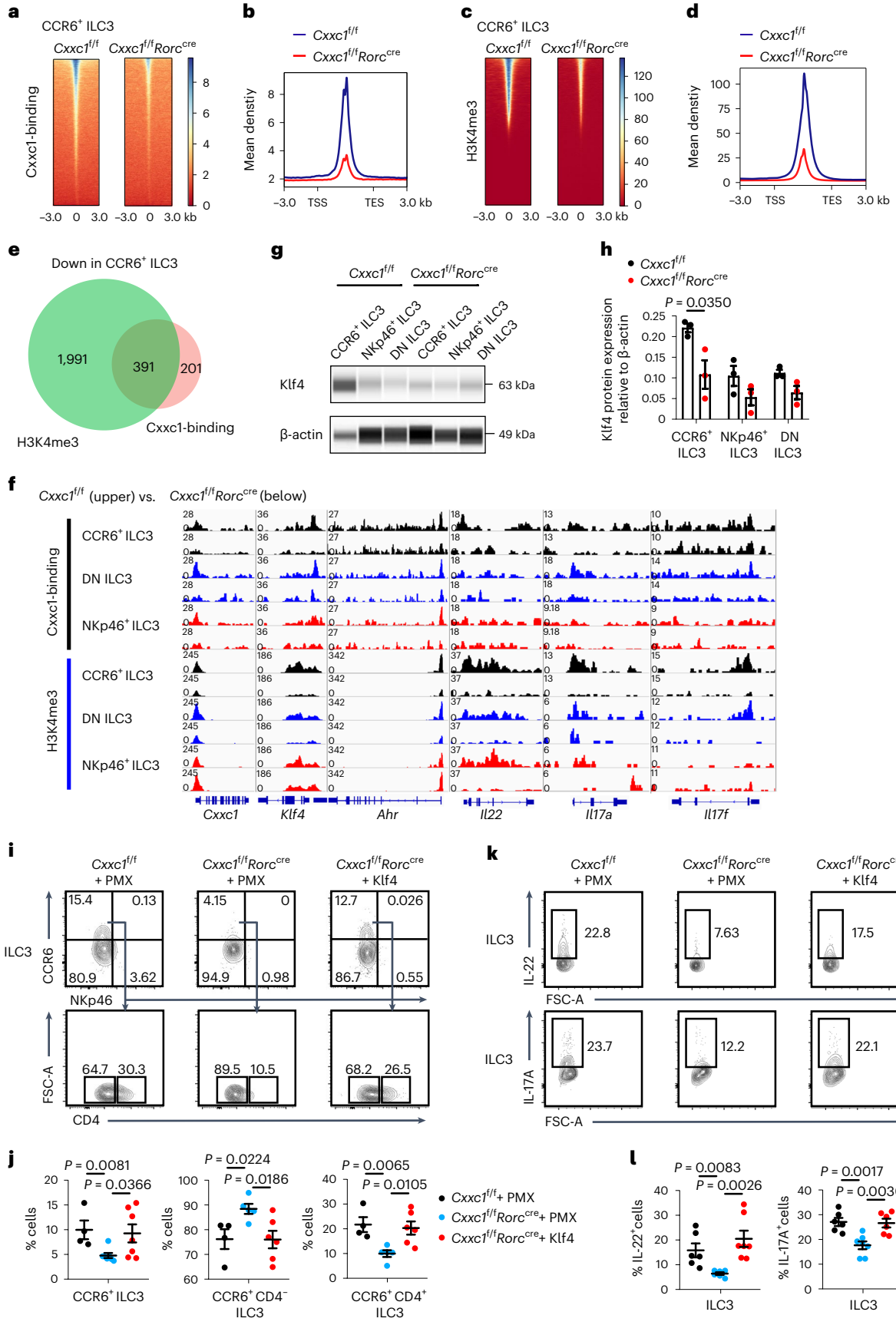

mock-transfected control (Fig. 7i,j). In addition, the overexpression of Klf4 restored CCR6$^+$CD4$^-$ and CCR6$^+$CD4$^+$ ILC3s populations. Notably, Cxxc1-deficient ILC3s derived from mock-transfected CLPs produced minimal IL-22 and IL-17A, whereas transfection with Klf4 led to high levels of production (Fig. 7k,l).

Additionally, we found that aged intestinal CCR6$^+$ ILC3s showed lower Klf4 expression than young mice (Extended Data Fig. 9a,b). The percentage of CCR6$^+$ ILC3s in the recipient mice that received Klf4-overexpressing CLPs from aged mice was higher than that in the control mice, and, similarly, the percentage of CCR6$^+$CD4$^+$ ILC3s was higher (Extended Data Fig. 9c,d). The overexpression of Klf4 increased the expression of IL-22 and IL-17A compared to that in ILC3s developed from mock-transfected CLPs in aged mice (Extended Data Fig. 9e,f).

Discussion

In the small intestine, we show that aging leads to deleterious effects on the homeostasis and function of ILC3s. LTi cells play a pivotal role in facilitating the formation of lymph nodes and PPs[56,57], and the possible role played by CCR6$^+$ ILC3s is evident only in early development, and its number and function decline with aging. In 2-week-old mice, NKp46$^+$ ILC3s start to populate[12,58], and many factors are involved in this period, including the microbiota[59], the Notch signaling pathway[18] and IL-23 production[12]. The ratio of CCR6$^-$NKp46$^-$ ILC3s, which are considered to contain precursors of NKp46$^+$ ILC3s, remains unchanged in aged gut. Based on the data showing that NKp46$^+$ ILC3s from aged donor cells remain largely unchanged, a hypothesis that the expansion of NKp46$^+$ ILC3s in aged mice is caused by environmental elements or metabolic alterations is reasonable. The secretion of IL-22 and IL-17A was impaired in ILC3s of aged mice, and the expression of AHR ligands that activate IL-22 release was also decreased. The recognition of AHR is a key regulator of homeostatic processes at barrier sites in the gut. Increasing evidence has revealed that AHR affects a wide array of tissue homeostasis functions and plays an important role in aging[60].

Multiple studies have suggested that histone modifications are the essential components of epigenetic regulation during aging[61–63]. In both human and mouse HSCs, the abundance of heterochromatin-related repressive histone mark H3K9me3 decreases with age[64]. The abundance of H4K20me3 increases with age in rat livers and senescent cells[65,66]. Among ILC3s, the differences in H3K4me3 abundance were predominantly found in CCR6$^+$ ILC3s, along with fewer H3K4me3 marks at most effector signature genes. Therefore, we propose that loss of Cxxc1-induced H3K4me3 marks contributes to cellular senescence in a cell-context-specific and a cell-type-specific manner. In addition, the histone H3K36 methyltransferase Setd2 was identified as critical for the maintenance and function of ILC3s because it supports CCR6 expression and restrains the generation of NKp46$^+$ ILC3s[67].

Klf4 was identified to function in the regulation of enhancer networks in cell fate transitions[68], including the epithelial-to-mesenchymal transition[69], monocyte cell differentiation[70] and the self-renewal and maintenance of the undifferentiated state of embryonic stem cells (ESCs)[71]. Recent reports have revealed that Klf4 was a key mediator in circadian immune regulation, as suggested by the ablation of Klf4 expression abolishing diurnal rhythms in phagocytic activity, indicating an association with age-dependent susceptibility to death caused by bacterial infection in aged macrophages[72].

In summary, our study reveals that epigenetic regulator Cxxc1 maintains H3K4me3 modification on genes, which is important for the homeostasis and function of ILC3s during aging.

Methods

Mice and ethics statement

The *Cxxc1*$^{f/f}$ mouse strain was described previously[33]. The *Rorc*^{cre} mice (JAX, 022791) were kindly provided by Ju Qiu (Shanghai Institutes for Biological Sciences, Chinese Academy of Sciences). *Cxxc1*$^{f/f}$ mice were crossed to *Rorc*^{cre} mice to generate respective conditional knockout mice. NOD Prkdc^{em26Cd52}Il2rg^{em26Cd22}/Nju (NCG, T001475) mice were purchased from Nanjing Biomedical Research Institute of Nanjing University. Mice were used at 6–8 weeks of age and kept co-housed after weaning. Young (6–8 weeks old) and aged (18 months old) mice of C57BL/6J background were obtained from Zhejiang University Laboratory Animal Center, as well as CD45.1 mice (2 months old). All mice were bred and maintained under specific pathogen-free conditions at the Zhejiang University Laboratory Animal Center, and all procedures involving animals were approved by the Zhejiang University Animal Care and Use Committee (approval no. ZJU20230177). The mice had free access to clean water and food. Animals were assigned experimental groups at random. Mice at 6–8 weeks of age were used for all experiments unless otherwise noted. The numbers and gender of mice per experimental group are indicated in the figure legends. All experiments were performed in accordance with the guidelines from the Animal Research and Ethics Boards of Zhejiang University.

Isolation of intestinal LPLs

LPLs were isolated from the small intestine as previously described[73]. In brief, small intestines were dissected, and fat tissues and PPs were removed. Intestines were dissected longitudinally and subsequently cut into 5mm-long pieces, followed by washing with DMEM. The intestinal pieces were then incubated in DMEM containing 3% FBS, 0.2% Hanks, 0.5 M EDTA and dithiothreitol (0.145 mg ml^{-1}) for 10 min with constant agitation by droppers. The tissues were then digested with DNase I (Sigma-Aldrich, 50 mg ml^{-1}) and collagenase II (Worthington-Biochem, 145 mg ml^{-1}) in DMEM at 37 °C for 5 min. The dissociated cells were filtered with a 100-µm cell strainer and harvested from the interphase of an 80% and 40% Percoll (GE Healthcare) gradient. After being washed with PBS and resuspended, LPLs were collected for further analysis.

Cell stimulation and flow cytometry

Cell stimulation was conducted as previously described[74].To evaluate cytokine expression, ex vivo LPLs were resuspended in DMEM with 50% FBS and then stimulated for 4 h at 37 °C with IL-23 (PeproTech, 40 ng ml^{-1}) and IL-1β (PeproTech, 20 ng ml^{-1}) for IL-22 production or with PMA (Sigma-Aldrich, 50 ng ml^{-1}) and ionomycin (Sigma-Aldrich, 1 mg ml^{-1}) for IL-17A and IFN-γ production. Then, 0.5 h after initiation of stimulation, a protein transport inhibitor, brefeldin A (BFA, 1000×, Invitrogen), was added to block cytokine secretion.

Dead cells were labeled with Fixable Viability Dye (eBioscience). Fc receptor blockade was performed using anti-CD16/32 (clone 93, BioLegend). For assessing bone marrow precursor cells, lineage staining included antibodies against TCRγδ, CD3ε, CD19, B220, NK1.1, CD11b, CD11c, Gr-1 and Ter119. For identifying peripheral ILCs, the lineage cocktail included TCRγδ, CD3ε, CD19, CD5, Gr-1 and Ter119. When intracellular transcription factor or cytocine staining was carried out, the cells were fixed and permeabilized with an Foxp3/transcription factor staining buffer set according to the manufacturer's instructions (Invitrogen) after staining for surface markers. Flow cytometry was performed with a BD Fortessa (BD Biosciences). Data were analyzed with FlowJo 10 software. Cells were sorted by an FACSAria II flow cytometer.

The following antibodies were purchased from eBioscience, Invitrogen, BD Biosciences or BioLegend: CD4 (RM4-5), IL-17A (TC11-18H10), CD27 (LG.7F9), CD25 (PC61.5), NK1.1 (PK136), IL-22 (IL22JOP), PLZF (9E12), CD45.2 (104), Ki67 (B56), RORgt (Q31-378), Flt3 (A2F10), IFN-γ (XMG-1.2), NKp46 (29A1.4), KLRG1 (2F1), CD127 (A7R34), CD117 (2B8), CCR6 (29-2L17), B220 (RA3-6B2), Sca-1 (D7), Isotype (P3.6.2.8.1), α4β7 (DATK32), CD45.1 (A20), AHR (4MEJJ) and streptavidin.

Bone marrow chimeras

CD45.2$^+$ bone marrow cells from young, aged, *Cxxc1*$^{f/f}$ or *Cxxc1*$^{f/f}$ *Rorc*^{cre} mice were mixed in a 1:1 ratio with CD45.1$^+$ wild-type bone marrow cells, respectively[75]. The mixture was intravenously injected into sublethally irradiated CD45.1$^+$ wild-type recipient mice. Eight weeks after cell transfer, we analyzed the intestinal ILC3s derived from CD45.2$^+$ donor cells by FACS.

S. typhimurium infection

S. typhimurium infection was conducted as previously described[73]. *Cxxc1*$^{f/f}$ and *Cxxc1*$^{f/f}$ *Rorc*^{cre} mice were fasted for 4 h and received 20 mg of streptomycin per mouse by oral gavage before being infected. Twenty hours later, they were orally inoculated with 1×10^9 CFUs of *S. typhimurium* (SL1344, SB300). All mice were sacrificed on day 4. Frequencies of NKp46$^+$ ILC3s from siLP were measured by flow cytometry.

C. rodentium infection

As previously described[74], *Cxxc1*$^{f/f}$ and *Cxxc1*$^{f/f}$ *Rorc*^{cre} mice (or young and aged mice) were orally inoculated with 5×10^9 CFUs of *C. rodentium* (DBS100) after being treated with ABX (autoclaved water supplemented with antibiotics: ampicillin 1 g L^{-1}, gentamicin 1 g L^{-1}, metronidazole 1 g L^{-1} and vancomycin 0.5 g L^{-1}) for 1 week. Body weight was monitored for 7 d, and all mice were sacrificed on day 7. Feces was collected to be weighed and plated on MacConkey agar plates to determine the colonies. The small intestines were used to isolate intestinal lymphocyte cells and analyzed for IL-22 production. The colons were measured for lengths and fixed for 24 h in 4% methanol for hematoxylin and eosin (H&E) staining.

C. albicans infection

As previously described[74], *C. albicans* strain SC5314 was grown in YPD (yeast nitrogen base with 2% glucose, 100 μg ml^{-1} ampicillin, 0.01 mg ml^{-1} vancomycin, 0.1 mg ml^{-1} centamicin). *C. albicans* (1×10^8 CFUs) was administered to *Cxxc1*$^{f/f}$ and *Cxxc1*$^{f/f}$ *Rorc*^{cre} mice (or young and aged mice) by gavage after 3-d ABX-1 (autoclaved water supplemented with streptomycin 2 mg ml^{-1}, fluconazole 0.2 mg ml^{-1} and gentamicin 0.2 mg ml^{-1}l) treatment. ABX-I was replaced with ABX-II (streptomycin 2 mg ml^{-1}, gentamicin 0.2 mg ml^{-1} and ampicillin 2 mg ml^{-1}) on day 3 and lasted until the end of the model. Body weight changes were monitored in the following 7 d, and all mice were sacrificed on day 11. Subsequent steps were consistent with the *C. rodentium* model, except for the identification of IL-17A expression.

Cell adoptive transfer into NCG mice

As previously described[74], NCG mice were adoptively transferred with 80,000 intestinal ILC3s (Lin$^-$CD127$^+$CD27$^-$KLRG1$^-$) sorted from *Cxxc1*$^{f/f}$ and *Cxxc1*$^{f/f}$ *Rorc*^{cre} mice (or young and aged mice) or PBS as control after treated with ABX for 1 week. ILC3s were stimulated with IL-23 and IL-1β for 30 min before being injected into NCG mice through the tail vein. NCG mice were orally inoculated with *C. rodentium* 24 h after adoptive transfer. Body weight was monitored for 9 d, and all mice were sacrificed for further analysis on day 9.

NCG mice were adoptively transferred with 80,000 intestinal ILC3s sorted from *Cxxc1*$^{f/f}$ and *Cxxc1*$^{f/f}$ *Rorc*^{cre} mice (or young and aged mice) or PBS as control after 3-d ABX-1 treatment. ILC3s were stimulated with PMA and ionomycin for 30 min before injected to NCG mice through the tail vein. ABX-I was replaced with ABX-II at day 3 and lasted until the end of the model. *C. albicans* was administered to NCG mice by gavage 24 h after adoptive transfer. Body weight changes were monitored for 9 d, and all mice were sacrificed for further analysis at day 9.

Hydrodynamic gene delivery of IL-22

Plasmid DNA was introduced into mice using a hydrodynamic tail vein injection-based gene transfer technique[76,77]. In brief, 10 μg of DNA/mouse was diluted in 1.5–2.0 ml of TransIT-EE Hydrodynamic Delivery Solution (MIR 5340, Mirus) at 0.1 ml g^{-1} body weight. The DNA solution was injected into mice through the tail vein using a 27-gauge needle within a time period of 5–10 s.

Histology

Colons were removed intact, fixed in 4% paraformaldehyde and embedded in paraffin, followed by sectioning and staining with H&E according to standard laboratory procedures.

Gene function of ILCs for in vivo analysis using retroviral transfection

Retroviruses were generated by transfection of pMX-IRES-GFP plasmids containing the indicated genes into Plat-E cells using PolyJet (SignaGen). Media were replaced 12/18 h after transfection, and retroviral supernatants were collected after 48 h. Then, 48-well plates were coated with RetroNectin (TaKaRa, 25 μg ml^{-1}) overnight at 4 °C. After blocking with BSA and washing, 1 ml of supernatant was added and followed by centrifugation for 2 h at 1,500*g* at 32 °C.

The bone marrow from *Cxxc1*$^{f/f}$ and *Cxxc1*$^{f/f}$ *Rorc*^{cre} mice (or young and aged mice) was aspirated to create a single-cell suspension[55]. CLPs (Lin$^-$CD127$^+$c-Kit^{int}Sca-1^{int}Flt3$^+$) were enriched by Dynabeads Biotin Binder (Invitrogen) after lineage staining and then superficially stained and sorted. We resuspended CLPs in CLP medium (αMEM medium containing 10% FBS, penicillin–streptomycin, 1× non-essential amino acids, 1 mM sodium pyruvate, 2 mM L-glutamine, 20 mM HEPES and 50 μM β-ME) and added 100,000 cells per well in the presence of IL-7 (20 ng ml^{-1}), IL-6 (10 ng ml^{-1}), SCF (100 ng ml^{-1}), Flt3L (20 ng ml^{-1}), TPO (10 ng ml^{-1}) and polybrene (Merck, 5 μg ml^{-1}). Ten hours later, retrovirus-transfected CLPs were collected and adoptively transferred into sublethally irradiated CD45.1$^+$ wild-type recipient mice through intravenous tail vein injection. Transduced cells were transferred with CD45.1$^+$ wild-type bone marrow cells to help the engraftment of the CLPs. After 2 weeks, recipient mice were sacrificed, and organs were collected for analysis.

Capillary western immunoassay

Protein extracts from 30,000 sorted CCR6$^+$ ILC3s (Lin$^-$CD127$^+$CD27$^-$KLRG1$^-$CCR6$^+$NKp46$^-$), NKp46$^+$ ILC3s (Lin$^-$CD127$^+$CD27$^-$KLRG1$^-$CCR6_NKp46$^+$) and DN ILC3s (Lin$^-$CD127$^+$CD27$^-$KLRG1$^-$CCR6$^-$NKp46$^-$) were prepared using cell lysis buffer (20% glycerol, 20 mM Tris-HCl pH 7.4, 0.5% NP40, 1 mM $MgCl_2$, 0.15 M NaCl,1 mM DTT, 1 mM EDTA, 1% SDS, 1 mM EGTA) with the addition of 1 mM PMSF and protein inhibitor cocktail. Protein concentration can be detected using the Qubit Protein Assay Kit (Invitrogen). Primary and secondary antibodies were diluted with Antibody Diluent II provided in the ProteinSimple kit (WM-W004-1). Immunoassay was performed using the Wes Simple Western method with the anti-rabbit detection module (ProteinSimple) according to the manufacturer's instructions. Protein expression was measured by the Compass for Simple Western program (ProteinSimple). Proteins were detected with the following primary antibodies: Cxxc1 (ab56035, Abcam) and Klf4 (PA5-23184, Invitrogen).

CUT&Tag and analysis

H3K4me3 and Cxxc1 Chip of three subsets of ILC3s were both performed on 100,000 cells as previously described with modifications according to the protocol of Hyperactive In-Situ ChIP Library Prep Kit for Illumina (TD 901, Vazyme)[78,79]. In brief, sorted CCR6$^+$ ILC3s, NKp46$^+$ ILC3s and DN ILC3s were washed with 500 μl of wash buffer containing 1× protease inhibitor cocktail (5056489001, Sigma-Aldrich). Cell pellets were resuspended in wash buffer. After two washes with binding buffer, Concanavalin A-coated magnetic beads were added and incubated at room temperature. Bead-bound cells were resuspended in 50 μl of antibody buffer. Then, 1 μg of H3K4me3 antibody (39016, Active Motif) and Cxxc1 antibody (ab198977, Abcam, provided by

Hengyu Fan, Institute of Life Sciences, Zhejiang University) was added and incubated overnight at 4 °C with slow rotation. After removing the primary antibody, the secondary antibody (goat anti-rabbit IgG, SAB3700883, Sigma-Aldrich) diluted in 50 µl of Dig-wash buffer at a ratio of 1:100 was added and incubated at room temperature. The cells were then incubated with 0.04 µM Hyperactive pG-Tn5 Transposase diluted in Dig-300 buffer at room temperature for 1 h with slow rotation. Finally, the cells were resuspended in tagmentation buffer and incubated at 37 °C for 1 h. DNA was purified using phenol-chloroform-isoamyl alcohol extraction and ethanol precipitation after terminating tagmentation. DNA library amplification was performed according to the instructions and washed with VAHTS DNA Clean Beads (Vazyme). Libraries were sequenced on an Illumina NovaSeq platform, and 150-bp paired-end reads were generated.

All raw sequence data were quality trimmed using fastp (version 0.19.7) and aligned to the mm10 mouse genome using Bowtie2 (version 2.3.5.1) with options '–local–very-sensitive-local–no-unal–nomixed–no-discordant–phred33 -I 10 -X 700'. PCR duplicates were removed using Picard MarkDuplicates (version 2.25.0). Peaks were called using MACS2 (version 2.2.7.1) with options 'q 0.05'. DeepTools2 software (version 3.5.1) was used to create the peaks density plot and heat map graph. Visualization of peak distribution along genomic regions of interested genes was performed with IGV. Genomic annotation was assigned using ChIPSeeker (version 1.28.3). Promoters were defined as follows: within 3,000 bp around the TSS. Differential expression analysis of two groups was performed using DESeq2 (version 1.30.1).

scRNA-seq

In total, 300,000 sort-purified ILC3s from *Cxxc1*$^{f/f}$ and *Cxxc1*$^{f/f}$ *Rorc*^{cre} (or young and aged mice) siLP were resuspended in BD Pharmingen Stain Buffer (FBS) (554656). The cells were labeled with sample tags using a BD Mouse Immune Single-Cell Multiplexing Kit (633793). Single-cell capture and cDNA synthesis were performed by the BD Rhapsody Single-Cell Analysis System. scRNA-seq libraries were constructed using a BD Rhapsody WTA Amplification Kit (633801) following a standard protocol provided by the manufacturer.

scRNA-seq data analysis

The fastq files were processed using the BD Rhapsody Targeted Analysis Pipeline on Seven Bridges. First, the read pair was removed if the mean base quality score was less than 20. Next, the filtered R1 reads were analyzed to identify the cell label sequences and unique molecular identifiers (UMIs). R2 reads were aligned to the mouse genome (mm10) using Bowtie2 (version 2.3.5.1)[80]. Then, valid reads were collapsed into a single raw molecule based on the same cell label, UMI sequence and gene. Recursive substation error correction (RSEC) was applied to correct sequencing and PCR errors of raw UMI counts. The RSEC-adjusted molecule matrices were used for downstream analysis. For quality control, cells with less than 25% mitochondrial UMI counts or fewer than 200 genes detected were filtered out.

We followed the Scanpy workflow[81] for downstream analyses. Specifically, we (1) applied the log1pCP10K normalization to the raw counts; (2) selected highly variable genes; (3) regressed out the effects of the total count per cell and the percentage of mitochondrial gene count; (4) calculated the first 50 principal components; (5) applied Harmony[82] to remove sample-level batch effects; (6) reduced the data dimension through uniform manifold approximation and projection (UMAP)[83]; (7) clustered the single cells using an unsupervised graph-based clustering algorithm, Leiden[84]; (8) identified cluster-specific marker genes using Student's *t*-test; and (9) annotated the clusters for their major cell type identities based on the expression patterns of literature-derived marker genes.

Finally, ILC3s were extracted from the integrated atlas by searching for the subset positive for Rorc but negative for Cd3d. Data of ILC3s were then reprocessed from the raw counts and sub-clustered to identify fine cell states, namely Ccr6$^+$, NKp46$^+$, DN and proliferative.

Differential abundance testing

To test for ILC3 cell state abundance differences between different mouse groups in an unbiased manner, we performed differential abundance analysis on single cells derived from young, old and *Cxxc1*$^{f/f}$ *Rorc*^{cre} mice using the milopy package (version 0.0.999)[85]. Specifically, cell neighborhoods were first defined on a *k*-nearest neighbors graph, and differential abundance testing was then performed for each neighborhood using a negative binomial general linear model framework.

Pseudo-bulk analysis

To suppress false-positive discoveries in differential expression (DE) analyses using single cells as data points for statistical testing, we employed a pseudo-bulk alternative[86]. In brief, for cells of a specific combination of a cell state and a mouse group, we first aggregated reads across biological replicates, transforming a genes-by-cells matrix to a genes-by-replicates matrix using matrix multiplication. Then, we ran DESeq2 (version 1.30.1)[87], which used a Wald test of the negative binomial model coefficients to compute the statistical significance.

Statistics and reproducibility

Statistical parameters, including the exact value of *n*, the definition of center, dispersion and precision measures and statistical significance, are reported in the figures and figure legends. *P* values less than 0.05 were considered significant. Data from these experiments are presented as mean values ± s.e.m. A two-tailed Student's *t*-test was performed for comparisons between two groups. All statistical analyses were performed using GraphPad Prism software (version 8, GraphPad Software). The same samples were not repeatedly measured, and no data points were excluded from the analysis. The confidence interval was set at 95% for statistical analysis. No statistical methods were used to predetermine sample sizes, but our sample sizes are similar to those reported in previous publications[73,74]. No randomization method was used to allocate animals to experimental groups. Data distribution was assumed to be normal, but this was not formally tested. Data collection and analysis were not performed blinded to the conditions of the experiments.

For animal experiments, no statistical methods were used to predetermine sample sizes, although sample sizes were consistent with those from previous studies[42,79]. No explicit randomization method was used to allocate animals to experimental groups, and mice were tested and data were processed by an investigator blinded to animal treatment identity.

Reporting summary

Further information on research design is available in the Nature Portfolio Reporting Summary linked to this article.

Data availability

This original data presented in the study can be found on the Gene Expression Omnibus—scRNA-seq (GSE208733, GSE210195, GSE210193 and GSE209592) and CUT&Tag (GSE211017 and GSE210194)—and are available from the corresponding authors upon reasonable request. Source data are provided with this paper.

Code availability

The scRNA-seq code used in this study is available in the GitHub repository at https://github.com/anjin8023/wanglab.git. The CUT&Tag code used in this study is available in the GitHub repository at https://github.com/anjin8023/wanglabCUTTag.git.

References

1. Nikolich-Zugich, J. The twilight of immunity: emerging concepts in aging of the immune system. *Nat. Immunol.* **19**, 10–19 (2018).
2. Ray, D. & Yung, R. Immune senescence, epigenetics and autoimmunity. *Clin. Immunol.* **196**, 59–63 (2018).
3. Sadighi Akha, A. A. Aging and the immune system: an overview. *J. Immunol. Methods* **463**, 21–26 (2018).
4. Hu, B. et al. Transcription factor networks in aged naive CD4 T cells bias lineage differentiation. *Aging Cell* **18**, e12957 (2019).
5. Mittelbrunn, M. & Kroemer, G. Hallmarks of T cell aging. *Nat. Immunol.* **22**, 687–698 (2021).
6. Dowery, R. et al. Peripheral B cells repress B-cell regeneration in aging through a TNF-α/IGFBP-1/IGF-1 immune-endocrine axis. *Blood* **138**, 1817–1829 (2021).
7. Goldberg, E. L., Shaw, A. C. & Montgomery, R. R. How inflammation blunts innate immunity in aging. *Interdiscip. Top. Gerontol. Geriatr.* **43**, 1–17 (2020).
8. Stotesbury, C. et al. Defective early innate immune response to ectromelia virus in the draining lymph nodes of aged mice due to impaired dendritic cell accumulation. *Aging Cell* **19**, e13170 (2020).
9. Fung, I. T. H. et al. Activation of group 2 innate lymphoid cells alleviates aging-associated cognitive decline. *J. Exp. Med.* **217**, e20190915 (2020).
10. Vivier, E. et al. Innate lymphoid cells: 10 years on. *Cell* **174**, 1054–1066 (2018).
11. Klose, C. S. & Artis, D. Innate lymphoid cells as regulators of immunity, inflammation and tissue homeostasis. *Nat. Immunol.* **17**, 765–774 (2016).
12. Klose, C. S. et al. A T-bet gradient controls the fate and function of CCR6^{-}RORγ^{+} innate lymphoid cells. *Nature* **494**, 261–265 (2013).
13. Melo-Gonzalez, F. & Hepworth, M. R. Functional and phenotypic heterogeneity of group 3 innate lymphoid cells. *Immunology* **150**, 265–275 (2017).
14. Mebius, R. E. Organogenesis of lymphoid tissues. *Nat. Rev. Immunol.* **3**, 292–303 (2003).
15. Meier, D. et al. Ectopic lymphoid-organ development occurs through interleukin 7-mediated enhanced survival of lymphoid-tissue-inducer cells. *Immunity* **26**, 643–654 (2007).
16. Robinette, M. L. et al. Transcriptional programs define molecular characteristics of innate lymphoid cell classes and subsets. *Nat. Immunol.* **16**, 306–317 (2015).
17. Zhong, C., Zheng, M. & Zhu, J. Lymphoid tissue inducer—a divergent member of the ILC family. *Cytokine Growth Factor Rev.* **42**, 5–12 (2018).
18. Rankin, L. C. et al. The transcription factor T-bet is essential for the development of NKp46^{+} innate lymphocytes via the Notch pathway. *Nat. Immunol.* **14**, 389–395 (2013).
19. Artis, D. & Spits, H. The biology of innate lymphoid cells. *Nature* **517**, 293–301 (2015).
20. Keir, M., Yi, Y., Lu, T. & Ghilardi, N. The role of IL-22 in intestinal health and disease. *J. Exp. Med.* **217**, e20192195 (2020).
21. Pagiatakis, C., Musolino, E., Gornati, R., Bernardini, G. & Papait, R. Epigenetics of aging and disease: a brief overview. *Aging Clin. Exp. Res.* **33**, 737–745 (2021).
22. Lopez-Otin, C., Blasco, M. A., Partridge, L., Serrano, M. & Kroemer, G. The hallmarks of aging. *Cell* **153**, 1194–1217 (2013).
23. Shchukina, I. et al. Enhanced epigenetic profiling of classical human monocytes reveals a specific signature of healthy aging in the DNA methylome. *Nat. Aging* **1**, 124–141 (2021).
24. Dozmorov, M. G., Coit, P., Maksimowicz-McKinnon, K. & Sawalha, A. H. Age-associated DNA methylation changes in naive CD4^{+} T cells suggest an evolving autoimmune epigenotype in aging T cells. *Epigenomics* **9**, 429–445 (2017).
25. McCauley, B. S. & Dang, W. Histone methylation and aging: lessons learned from model systems. *Biochim. Biophys. Acta* **1839**, 1454–1462 (2014).
26. Hsu, C. L., Lo, Y. C. & Kao, C. F. H3K4 methylation in aging and metabolism. *Epigenomes* **5**, 14 (2021).
27. Sen, P., Shah, P. P., Nativio, R. & Berger, S. L. Epigenetic mechanisms of longevity and aging. *Cell* **166**, 822–839 (2016).
28. Sun, D. et al. Epigenomic profiling of young and aged HSCs reveals concerted changes during aging that reinforce self-renewal. *Cell Stem Cell* **14**, 673–688 (2014).
29. Thomson, J. P. et al. CpG islands influence chromatin structure via the CpG-binding protein Cfp1. *Nature* **464**, 1082–1086 (2010).
30. Yang, Y., Yang, Y., Chan, K. & Couture, J. F. Analyzing the impact of CFP1 mutational landscape on epigenetic signaling. *FASEB J.* **35**, e21790 (2021).
31. Sha, Q. Q. et al. CFP1-dependent histone H3K4 trimethylation in murine oocytes facilitates ovarian follicle recruitment and ovulation in a cell-nonautonomous manner. *Cell. Mol. Life Sci.* **77**, 2997–3012 (2020).
32. Sha, Q. Q. et al. Role of CxxC-finger protein 1 in establishing mouse oocyte epigenetic landscapes. *Nucleic Acids Res.* **49**, 2569–2582 (2021).
33. Cao, W. et al. CXXC finger protein 1 is critical for T-cell intrathymic development through regulating H3K4 trimethylation. *Nat. Commun.* **7**, 11687 (2016).
34. Chun, K. T. et al. The epigenetic regulator CXXC finger protein 1 is essential for murine hematopoiesis. *PLoS ONE* **9**, e113745 (2014).
35. Lin, F. et al. Epigenetic initiation of the T_H17 differentiation program is promoted by Cxxc finger protein 1. *Sci. Adv.* **5**, eaax1608 (2019).
36. Hui, Z. et al. Cxxc finger protein 1 positively regulates GM-CSF-derived macrophage phagocytosis through Csf2rα-mediated signaling. *Front. Immunol.* **9**, 1885 (2018).
37. Bilmez, Y., Talibova, G. & Ozturk, S. Expression of the histone lysine methyltransferases SETD1B, SETDB1, SETD2, and CFP1 exhibits significant changes in the oocytes and granulosa cells of aged mouse ovaries. *Histochem. Cell Biol.* **158**, 79–95 (2022).
38. Verrier, T. et al. Phenotypic and functional plasticity of murine intestinal NKp46^{+} group 3 innate lymphoid cells. *J. Immunol.* **196**, 4731–4738 (2016).
39. Viant, C. et al. Transforming growth factor-β and Notch ligands act as opposing environmental cues in regulating the plasticity of type 3 innate lymphoid cells. *Sci. Signal.* **9**, ra46 (2016).
40. Shih, H. Y. et al. Developmental acquisition of regulomes underlies innate lymphoid cell functionality. *Cell* **165**, 1120–1133 (2016).
41. Rutz, S., Eidenschenk, C. & Ouyang, W. IL-22, not simply a Th17 cytokine. *Immunol. Rev.* **252**, 116–132 (2013).
42. Sanos, S. L., Vonarbourg, C., Mortha, A. & Diefenbach, A. Control of epithelial cell function by interleukin-22-producing RORγt^{+} innate lymphoid cells. *Immunology* **132**, 453–465 (2011).
43. Sonnenberg, G. F., Monticelli, L. A., Elloso, M. M., Fouser, L. A. & Artis, D. CD4^{+} lymphoid tissue-inducer cells promote innate immunity in the gut. *Immunity* **34**, 122–134 (2011).
44. Collins, J. W. et al. Citrobacter rodentium: infection, inflammation and the microbiota. *Nat. Rev. Microbiol.* **12**, 612–623 (2014).
45. Silberger, D. J., Zindl, C. L. & Weaver, C. T. *Citrobacter rodentium*: a model enteropathogen for understanding the interplay of innate and adaptive components of type 3 immunity. *Mucosal Immunol.* **10**, 1108–1117 (2017).
46. Gladiator, A., Wangler, N., Trautwein-Weidner, K. & LeibundGut-Landmann, S. Cutting edge: IL-17-secreting innate lymphoid cells are essential for host defense against fungal infection. *J. Immunol.* **190**, 521–525 (2013).

47. Busuttil, R., Bahar, R. & Vijg, J. Genome dynamics and transcriptional deregulation in aging. *Neuroscience* **145**, 1341–1347 (2007).
48. Sun, L., Yu, R. & Dang, W. Chromatin architectural changes during cellular senescence and aging. *Genes (Basel)* **9**, 211 (2018).
49. Shilatifard, A. The COMPASS family of histone H3K4 methylases: mechanisms of regulation in development and disease pathogenesis. *Annu. Rev. Biochem.* **81**, 65–95 (2012).
50. Eberl, G. & Littman, D. R. Thymic origin of intestinal αβ T cells revealed by fate mapping of RORγ$^+$ cells. *Science* **305**, 248–251 (2004).
51. Kondo, M., Weissman, I. L. & Akashi, K. Identification of clonogenic common lymphoid progenitors in mouse bone marrow. *Cell* **91**, 661–672 (1997).
52. Seillet, C. et al. Deciphering the innate lymphoid cell transcriptional program. *Cell Rep.* **17**, 436–447 (2016).
53. Harly, C., Cam, M., Kaye, J. & Bhandoola, A. Development and differentiation of early innate lymphoid progenitors. *J. Exp. Med.* **215**, 249–262 (2018).
54. Qiu, J. et al. The aryl hydrocarbon receptor regulates gut immunity through modulation of innate lymphoid cells. *Immunity* **36**, 92–104 (2012).
55. Seillet, C. & Belz, G. T. Assessment of gene function of mouse innate lymphoid cells for in vivo analysis using retroviral transduction. *Methods Mol. Biol.* **1953**, 231–240 (2019).
56. Buettner, M. & Lochner, M. Development and function of secondary and tertiary lymphoid organs in the small intestine and the colon. *Front. Immunol.* **7**, 342 (2016).
57. Stehle, C. et al. T-bet and RORα control lymph node formation by regulating embryonic innate lymphoid cell differentiation. *Nat. Immunol.* **22**, 1231–1244 (2021).
58. Sawa, S. et al. Lineage relationship analysis of RORγt$^+$ innate lymphoid cells. *Science* **330**, 665–669 (2010).
59. Sanos, S. L. et al. RORgammat and commensal microflora are required for the differentiation of mucosal interleukin 22-producing NKp46$^+$ cells. *Nat. Immunol.* **10**, 83–91 (2009).
60. Yang, C. E. et al. Aryl hydrocarbon receptor: from pathogenesis to therapeutic targets in aging-related tissue fibrosis. *Ageing Res. Rev.* **79**, 101662 (2022).
61. He, J., Kallin, E. M., Tsukada, Y. & Zhang, Y. The H3K36 demethylase Jhdm1b/Kdm2b regulates cell proliferation and senescence through p15^{Ink4b}. *Nat. Struct. Mol. Biol.* **15**, 1169–1175 (2008).
62. Tanaka, H. et al. The SETD8/PR-Set7 methyltransferase functions as a barrier to prevent senescence-associated metabolic remodeling. *Cell Rep.* **18**, 2148–2161 (2017).
63. Greer, E. L. et al. Members of the H3K4 trimethylation complex regulate lifespan in a germline-dependent manner in *C. elegans*. *Nature* **466**, 383–387 (2010).
64. Djeghloul, D. et al. Age-associated decrease of the histone methyltransferase SUV39H1 in HSC perturbs heterochromatin and B lymphoid differentiation. *Stem Cell Rep.* **6**, 970–984 (2016).
65. Fraga, M. F. & Esteller, M. Epigenetics and aging: the targets and the marks. *Trends Genet.* **23**, 413–418 (2007).
66. Sarg, B., Koutzamani, E., Helliger, W., Rundquist, I. & Lindner, H. H. Postsynthetic trimethylation of histone H4 at lysine 20 in mammalian tissues is associated with aging. *J. Biol. Chem.* **277**, 39195–39201 (2002).
67. Chang, J. et al. Setd2 determines distinct properties of intestinal ILC3 subsets to regulate intestinal immunity. *Cell Rep.* **38**, 110530 (2022).
68. Kapoor, N. et al. Transcription factors STAT6 and KLF4 implement macrophage polarization via the dual catalytic powers of MCPIP. *J. Immunol.* **194**, 6011–6023 (2015).
69. Liao, X. et al. Kruppel-like factor 4 regulates macrophage polarization. *J. Clin. Invest.* **121**, 2736–2749 (2011).
70. Dykstra, B. & de Haan, G. Hematopoietic stem cell aging and self-renewal. *Cell Tissue Res.* **331**, 91–101 (2008).
71. Li, Y. et al. Murine embryonic stem cell differentiation is promoted by SOCS-3 and inhibited by the zinc finger transcription factor Klf4. *Blood* **105**, 635–637 (2005).
72. Blacher, E. et al. Aging disrupts circadian gene regulation and function in macrophages. *Nat. Immunol.* **23**, 229–236 (2022).
73. Yin, S. et al. Runx3 mediates resistance to intracellular bacterial infection by promoting IL12 signaling in group 1 ILC and NCR$^+$ILC3. *Front. Immunol.* **9**, 2101 (2018).
74. Gao, X. et al. The transcription factor ThPOK regulates ILC3 lineage homeostasis and function during intestinal infection. *Front. Immunol.* **13**, 939033 (2022).
75. Tizian, C. et al. c-Maf restrains T-bet-driven programming of CCR6-negative group 3 innate lymphoid cells. *eLife* **9**, e52549 (2020).
76. Herweijer, H. & Wolff, J. A. Progress and prospects: naked DNA gene transfer and therapy. *Gene Ther.* **10**, 453–458 (2003).
77. Knapp, J. E. & Liu, D. Hydrodynamic delivery of DNA. *Methods Mol. Biol.* **245**, 245–250 (2004).
78. Kaya-Okur, H. S. et al. CUT&Tag for efficient epigenomic profiling of small samples and single cells. *Nat. Commun.* **10**, 1930 (2019).
79. Dan, L. et al. The phosphatase PAC1 acts as a T cell suppressor and attenuates host antitumor immunity. *Nat. Immunol.* **21**, 287–297 (2020).
80. Langmead, B. & Salzberg, S. L. Fast gapped-read alignment with Bowtie 2. *Nat. Methods* **9**, 357–359 (2012).
81. Wolf, F. A., Angerer, P. & Theis, F. J. SCANPY: large-scale single-cell gene expression data analysis. *Genome Biol.* **19**, 15 (2018).
82. Korsunsky, I. et al. Fast, sensitive and accurate integration of single-cell data with Harmony. *Nat. Methods* **16**, 1289–1296 (2019).
83. McInnes, L., Healy, J. & Melville, J. UMAP: uniform manifold approximation and projection for dimension reduction. Preprint at *arXiv* https://doi.org/10.48550/arXiv.1802.03426 (2018).
84. Traag, V. A., Waltman, L. & van Eck, N. J. From Louvain to Leiden: guaranteeing well-connected communities. *Sci. Rep.* **9**, 5233 (2019).
85. Dann, E., Henderson, N. C., Teichmann, S. A., Morgan, M. D. & Marioni, J. C. Differential abundance testing on single-cell data using *k*-nearest neighbor graphs. *Nat. Biotechnol.* **40**, 245–253 (2022).
86. Squair, J. W. et al. Confronting false discoveries in single-cell differential expression. *Nat. Commun.* **12**, 5692 (2021).
87. Love, M. I., Huber, W. & Anders, S. Moderated estimation of fold change and dispersion for RNA-seq data with DESeq2. *Genome Biol.* **15**, 550 (2014).

Acknowledgements

We thank J. Qiu (Shanghai Institute of Biochemistry and Cell Biology, Chinese Academy of Sciences) for her generous gifts of *C. rodentium*. We thank H. Guanghua (Fudan University) for his generous gifts of *C. albicans*. We thank Y. Q. Zhu (Zhejiang University) for providing *S. typhimurium* (SL1344, SB300). We thank X. Guo (Institute of Immunology, Tsinghua University School of Medicine) for providing pRK-mIL-22 and control vector (pRK). We thank Y. Li, Y. Huang and W. Yin from the Core Facilities, Zhejiang University School of Medicine, for their technical support. We thank Y. Ding, H. Jin and X. Zhang from Animal Facilities, Zhejiang University, for mice maintenance. This work was supported by grants from the National Natural Science Foundation of China (nos. 32030035, 91442101 and 32100693), the Zhejiang Provincial Natural Science Foundation of China (no. LZ21C080001), Science and Technology Innovation 2030-Major Project (2021ZD0200405), Key Project of Experimental Technology Program of Zhejiang University (no. SZD202203) and Pre-research Projects of Innovation Center of Yangtze River Delta,

Zhejiang University (no. 2022ZY008). The funders had no role in study design, data collection and analysis, decision to publish or preparation of the manuscript.

Author contributions

L.W., H.L. and C.W.: supervision, conceptualization, project administration and writing—review and editing. L.L. and D.W.: writing—review and editing. L.W.: funding acquisition. X.S. and X.G.: investigation, methodology, project administration and writing—original draft. X.G. and Y.L.: data curation and formal analysis. Q.X., Y.F., S.H., Z.H., X.L., Q.W. and Z.C.: investigation and methodology.

Competing interests

The authors declare no competing interests.

Additional information

Extended data is available for this paper at https://doi.org/10.1038/s43587-023-00453-7.

Supplementary information The online version contains supplementary material available at https://doi.org/10.1038/s43587-023-00453-7.

Correspondence and requests for materials should be addressed to Chuan Wu, Han Liang or Lie Wang.

Peer review information *Nature Aging* thanks David Withers, Jörg Fritz and the other, anonymous, reviewers for their contribution to the peer review of this work.

https://doi.org/10.1038/s43587-023-00453-7

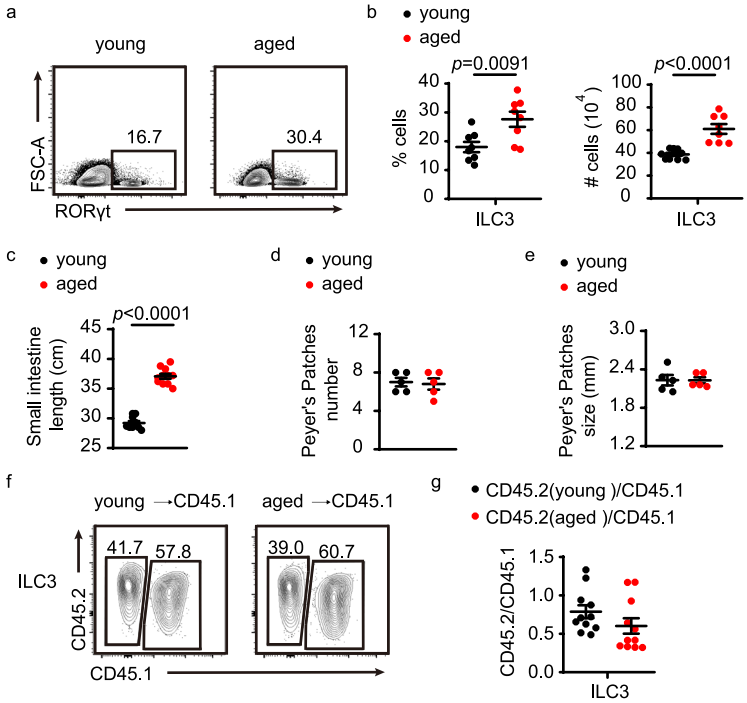

Extended Data Fig. 1 | Phenotype of ILC3s in the intestine of aged mice. (a) Flow cytometry of Lin$^-$RORγt$^+$ ILC3s isolated from the siLP of young and aged mice. (b) The percentages (n = 8) and total numbers of ILC3s were compared (n = 10 young, n = 8 aged). (c) Summary of small intestine lengths in young and aged mice (n = 10 young, n = 11 aged). (d, e) The numbers and size of Peyer's patches in the small intestine of young and aged mice were compared (n = 5). (f) Flow cytometric analysis of CD45.1 and CD45.2 expression in ILC3s. (g) The percentages of donor-derived cells shown in (f) (CD45.2/CD45.1) were compared (n = 11). Bar graphs are presented as mean ± SEM. A two-tailed Student's t-test was performed for comparisons. The data are representative of at least three independent experiments (a-g).

https://doi.org/10.1038/s43587-023-00453-7

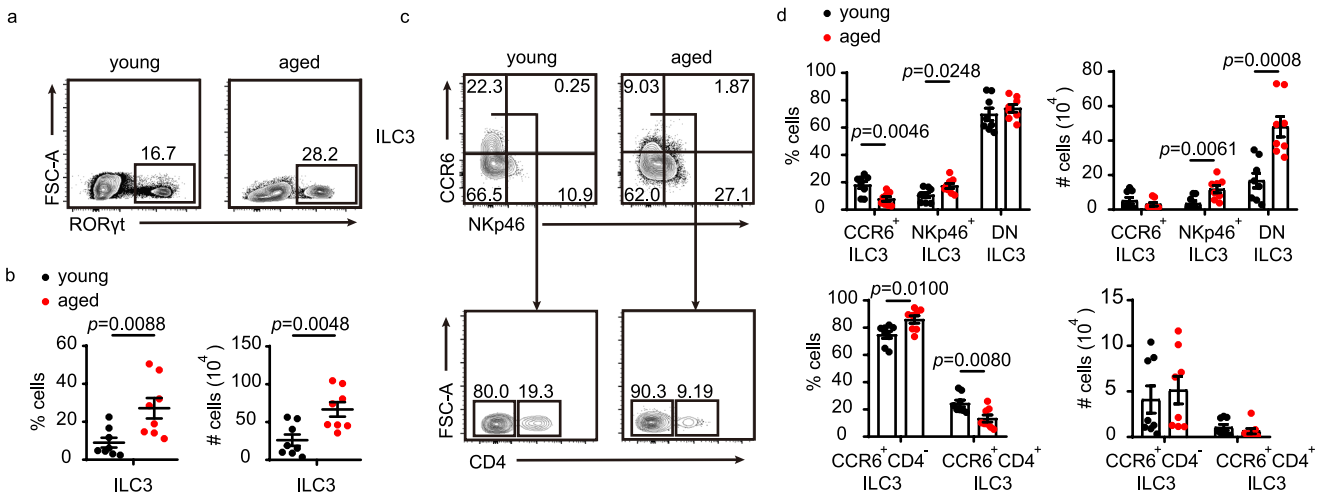

Extended Data Fig. 2 | Phenotype of aged gut CCR6+ ILC3s is not affected by gender. (a) Flow cytometry of ILC3s from the siLP of young (6- to 8-week-old, female) and aged mice (18-month-old, female). All data showed above gated out Lin$^+$ cells in advance. (b) The percentages and total numbers of ILC3s were compared (n = 8). (c) The Lin$^-$RORγt$^+$ ILC3s shown in (a) were further characterized based on their CCR6 and NKp46 expression (upper). The CD4$^+$ ILC3 subset among the CCR6$^+$ ILC3s was analyzed (below). (d) The percentages and total numbers of all subsets were (n = 8). Bar graphs are presented as mean ± SEM. A two-tailed Student's t-test was performed for comparisons. The data are representative of four independent experiments (a-d).

https://doi.org/10.1038/s43587-023-00453-7

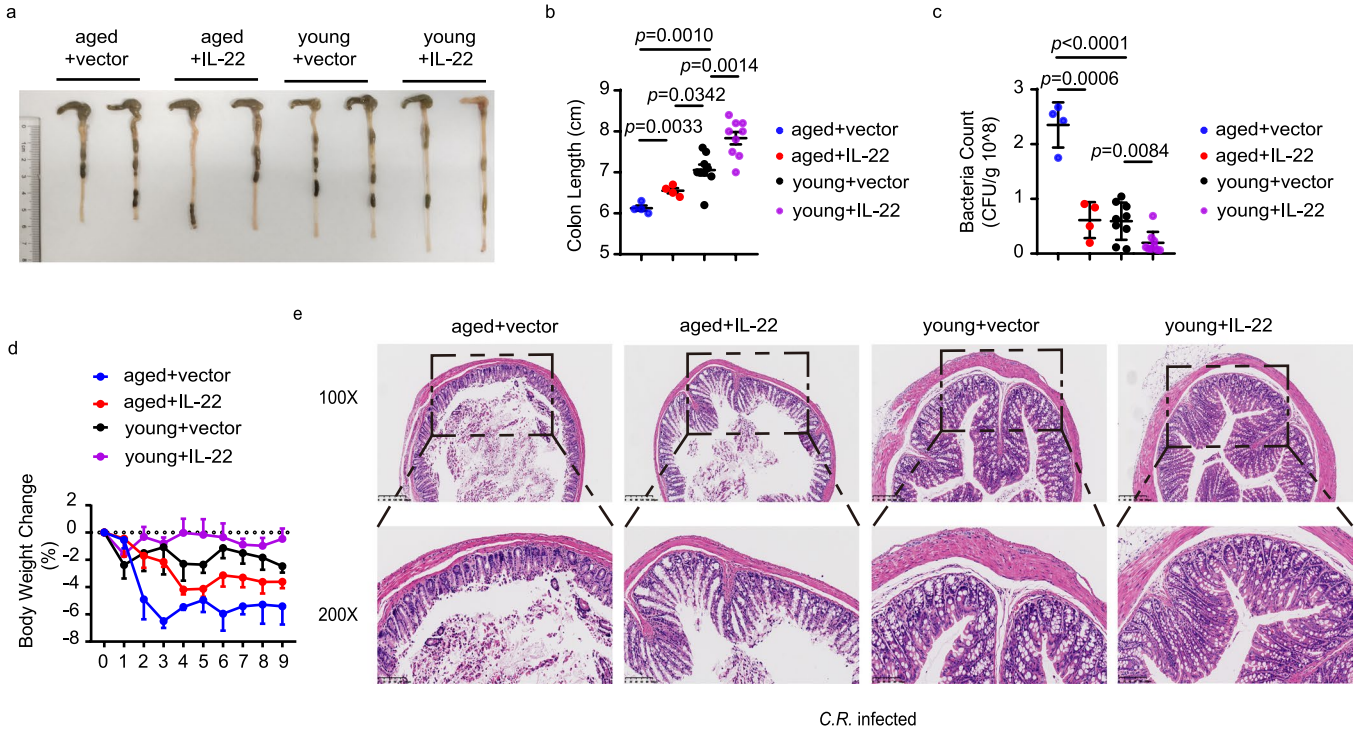

Extended Data Fig. 3 | Ectopic expression of IL-22 protects aged mice from C. rodentium infection. (a-e) young (6- to 8-week-old, male) and aged mice (18-month-old, male) were infected with *C.rodentium*. Six hours after infection, IL-22-expressing plasmid (pRK-mIL-22) or control vector (pRK) was administered into the mice via hydrodynamic injection. (a, b) Colon lengths of young and aged mice (n = 9 young, n = 4 aged). (c) Bacterial counts in faeces (n = 9 young, n = 4 aged). (d) Body weight changes were monitored at the indicated time points (n = 3 aged+vector and aged+IL-22, n = 4 young+vector, n = 5 young+IL-22). (e) H&E staining of colon tissue sections. Bar graphs are presented as mean ± SEM. A two-tailed Student's t-test was performed for comparisons. Data are representative of two independent experiments (a-e).

https://doi.org/10.1038/s43587-023-00453-7

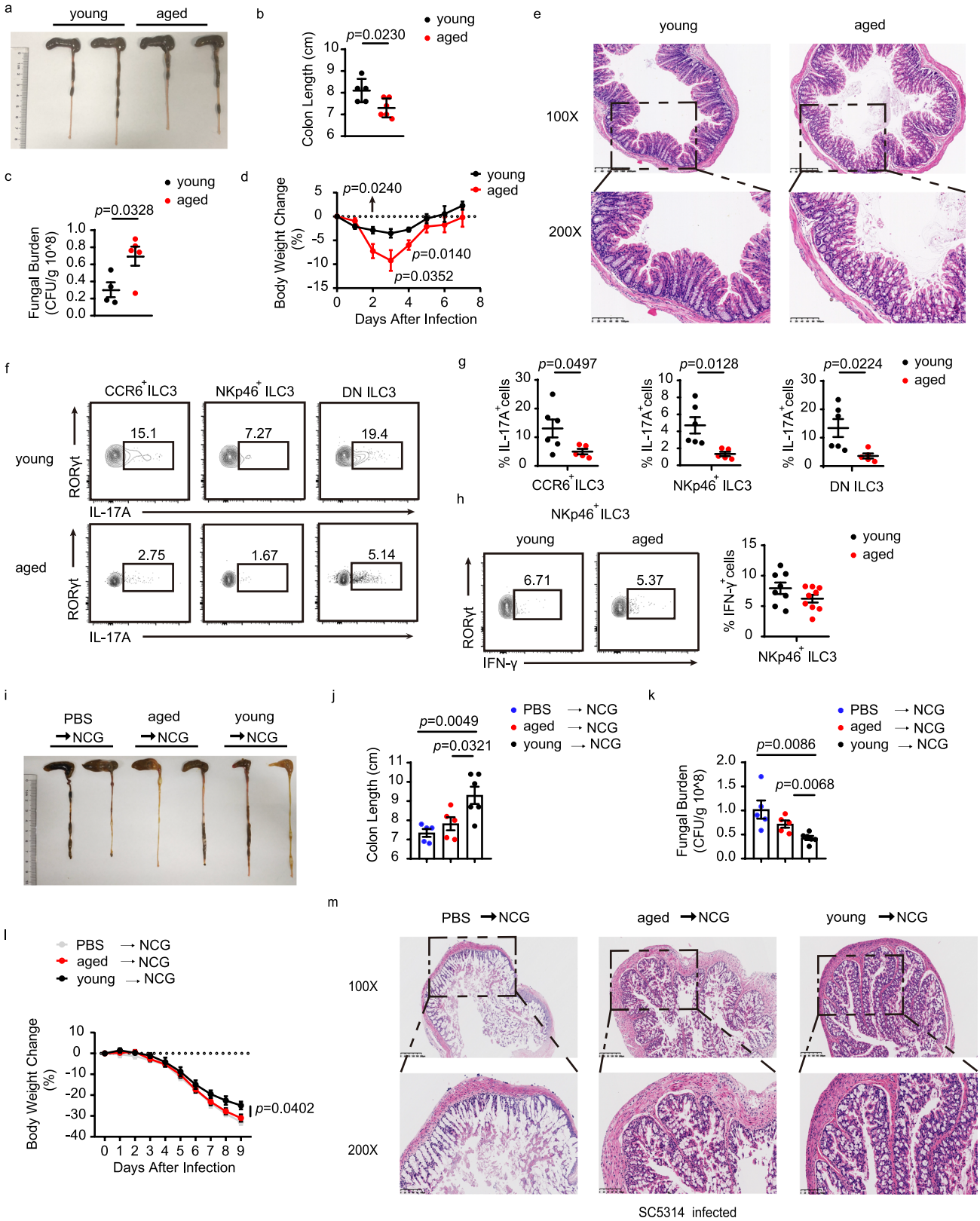

Extended Data Fig. 4 | See next page for caption.

https://doi.org/10.1038/s43587-023-00453-7

Extended Data Fig. 4 | Defective ILC3 function in aged mice compromises host defense against C. albicans infection. (a-g) *C. albicans* infection model. (a) Representative image of colons in young and aged mice after *C. albicans* infection on day 7. (b) Colon lengths were counted and plotted in infected mice (n = 5 young, n = 6 aged). (c) Colonies of *C. albicans* in the faeces were counted by serial dilution (n = 4 young, n = 5 aged). (d) Body weight changes (n = 6). (e) H&E-stained sections of representative colons. (f) Flow cytometric analysis of IL-17A expression in the indicated subsets 7 days after infection. (g) The percentages of IL-17A$^+$ cells were compared (n = 6 young, n = 5 aged). (h) Flow cytometric analysis of IFN-γ expression in NKp46$^+$ ILC3s after stimulation with PMA and ionomycin (left); right, quantification (n = 8 young, n = 9 aged). (i-m) ILC3s (Lin$^-$CD127$^+$CD27$^-$KLRG1$^-$) from young and aged mice were adoptively transferred into NCG mice with *C. albicans* infection. (i-j) Measurements and statistical analysis of the colon lengths from NCG recipients (n = 5 control and aged transferred, n = 6 young transferred). (k) CFUs in the faeces of NCG recipients 9 days after infection (n = 5 control and aged transferred, n = 6 young transferred). (l) Changes in body weight were recorded at the indicated time points (n = 5 control, n = 7 young transferred, n = 8 aged transferred). (m) Histological analysis of colonic tissues by H&E staining. The data are representative of two independent experiments. Bar graphs are presented as mean ± SEM. A two-tailed Student's t-test was performed for comparisons. The data are representative of three independent experiments (a-h) and two independent experiments (i-m).

https://doi.org/10.1038/s43587-023-00453-7

a

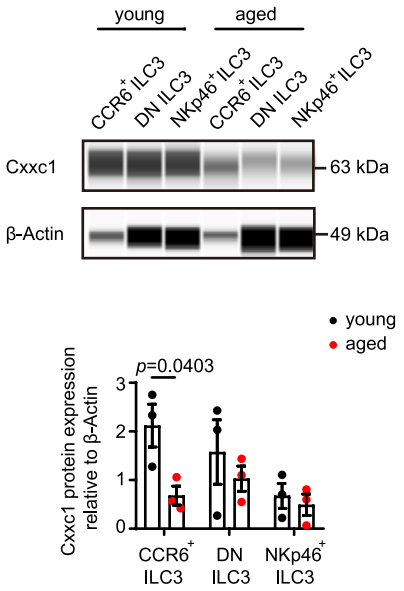

b

Srpx2	Lrba	Cep162	Ednra	Spaar
Sod3	Frem1	Ms4a4d	Mmp16	Schip1
Kcnt2	Fbln7	Med15	Ano5	Asxl3
Slc38a4	Mgp	Enpp3	Rerg	Svep1
Sash1	Frmd4b	Aspn	Rbm46os	Sfrp1
Fgd4	Tmem196	Sorl1	C1qtnf7	Pum3
Camk1g	Rassf6	Xirp2	Ptprd	Carmn
Dclk1	Cdh11	Tfpi2	Nap1l5	Steap2
Usp13	Greb1l	St3gal3	Sertm1	Kcnk2
Dcn	Fibin	Twist2	Eva1a	5730596B20Rik
Lepr	Fam118b	Adamts19	Rspo3	Tcaf1
Cyp7b1	Mtus1	Adcy2	Ccl11	Mir6417
Gm10471	Lgi2	Ereg	Nsg1	Pdpn
Lrrc55	Col6a5	Rspo2	Fgfr2	Abca8a
Dnah7b	F2rl1	Ror2	Fgf10	Itga11
Nox4	Mir700	Fmo2	Spon1	Lox
Tmem74	Cfh	Rgs6	Agtr1a	Acss3
Naaladl2	Tns1	Tspan11	Scara3	Col14a1
Srpx	Slit2	Kcnn3	Lrfn3	Negr1
Tenm3	Tcf21	Pdzrn3	Dpt	Pde3a

c

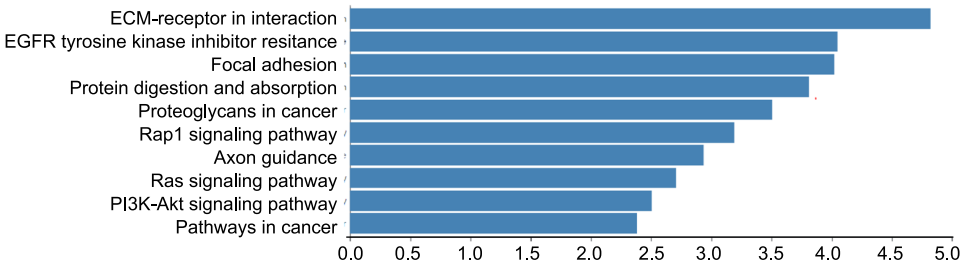

d control (upper) VS aged (below)

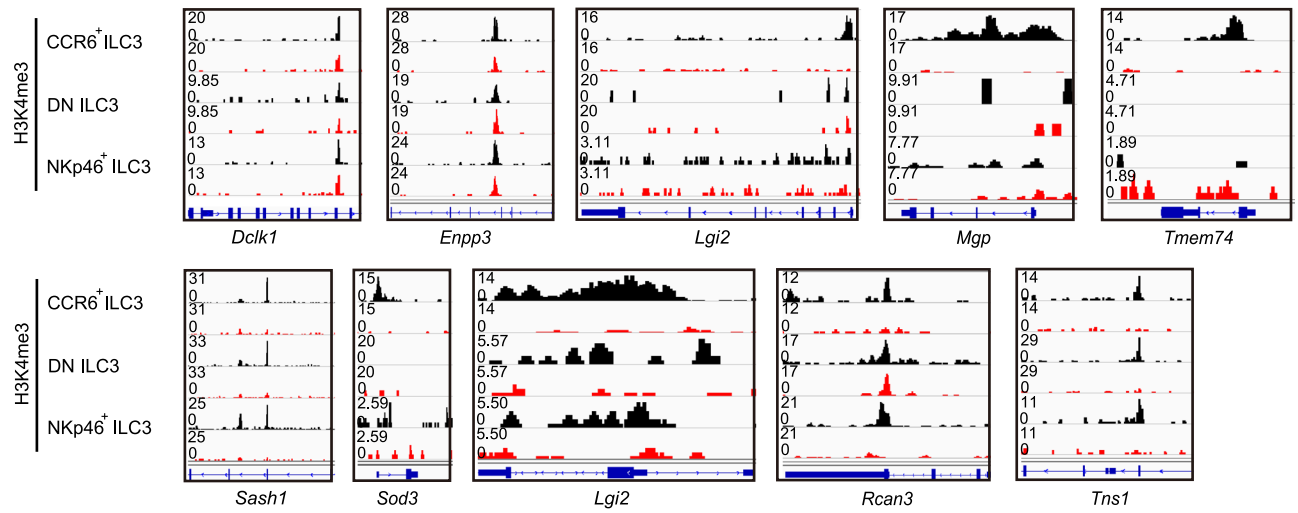

Extended Data Fig. 5 | Protein level of Cxxc1 and differentially H3K4me3 modified genes of intestinal ILC3s in aged mice. (a) Immunoblot images showing Cxxc1 protein in ILC3s sorted from young and aged mice (left). The relative protein content was normalized to β-Actin (right) (n = 3). (b-d) Anti H3K4me3 CUT&Tag in young mice versus aged mice. (b) Table showing top 100 genes with down-regulated H3K4me3 modification regions in aged mice. (c) KEGG pathway enrichment analysis performed by using DAVID. The top 10 highly enriched KEGG pathways are presented. (d) IGV visualizing keys genes related to pathways shown in (c). Bar graphs are presented as mean ± SEM. A two-tailed Student's t-test was performed for comparisons. The data are representative of three independent experiments (a).

https://doi.org/10.1038/s43587-023-00453-7

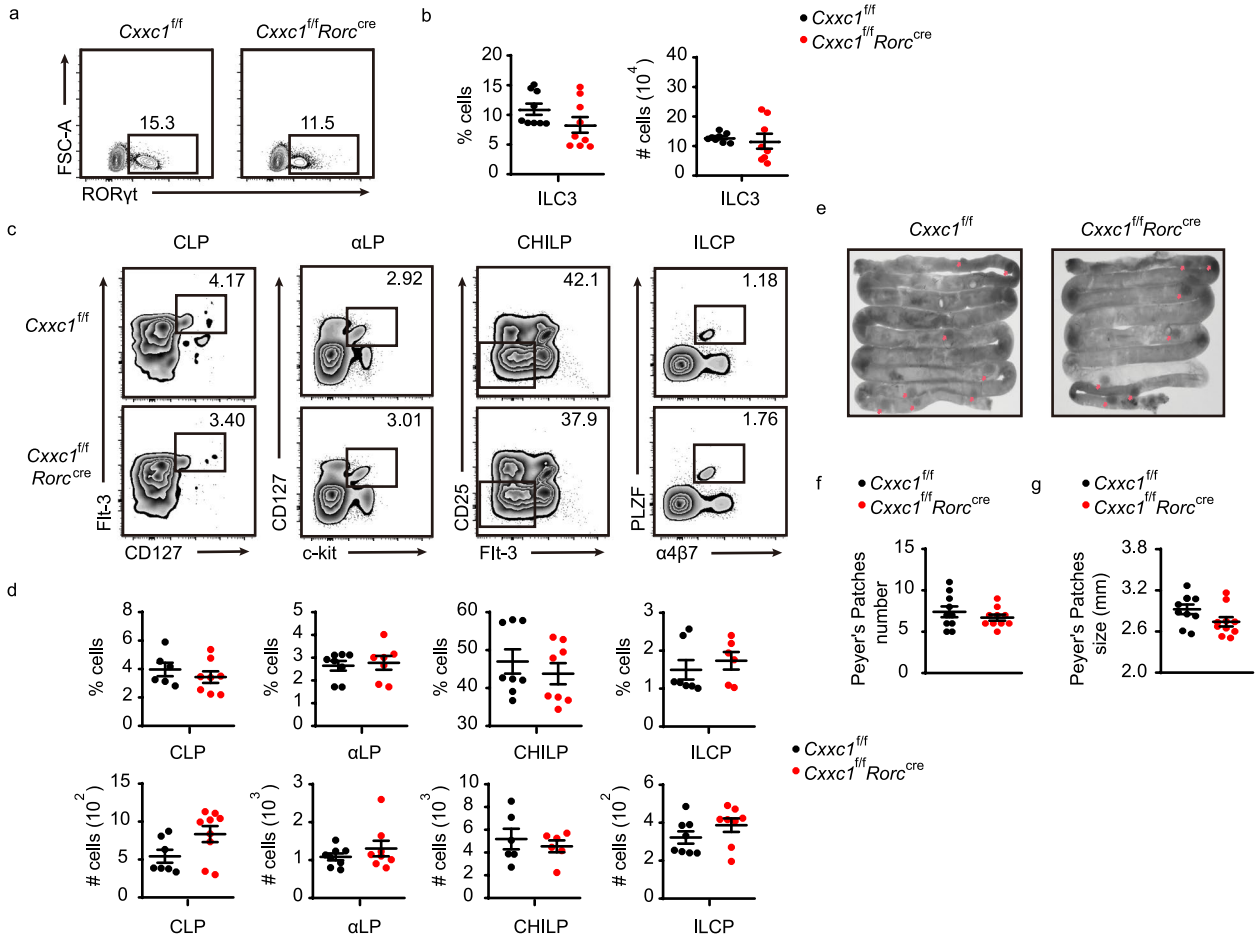

Extended Data Fig. 6 | Development of ILC progenitor in the bone marrow and formation of Peyer's patches are not affected in Cxxc1f/f RorcCre mice. (a) Flow cytometry of ILC3s from the siLP in *Cxxc1*$^{f/f}$ *Rorc*^{Cre} and *Cxxc1*$^{f/f}$ mice. All data showed above gated out Lin$^+$ cells in advance. (b) The percentages (n = 9) and total numbers (n = 8) of ILC3s were compared. (c) Flow cytometric analysis of common lymphoid progenitors (CLPs, Lin$^-$CD127$^+$c-Kit^{int}Sca1^{int}Flt3$^+$); α4β7$^+$ lymphoid progenitors (α-LPs, Lin$^-$CD127$^+$c-Kit$^+$α4β7$^+$); common helper-like innate lymphoid progenitors (ChILPs, Lin$^-$CD127$^+$α4β7$^+$CD25$^-$Flt3$^-$) and common ILC precursors (ILCPs, Lin$^-$CD127$^+$α4β7$^+$PLZF$^+$) in bone marrow in *Cxxc1*$^{f/f}$ *Rorc*^{Cre} mice and their wild-type *Cxxc1*$^{f/f}$ littermates. The lineage cocktail included TCRγδ, CD3ε, CD19, B220, NK1.1, CD11b, CD11c, Gr-1 and Ter119. (d) The percentages of CLPs, α-LPs, ChILPs, and ILCPs were compared. CLP (n = 6 WT, n = 8 KO), α-LP (n = 8 WT, n = 7 KO), ChILP (n = 8 WT, n = 8 KO), and ILCP (n = 7 WT, n = 6 KO). The cell numbers were compared. CLP (n = 7 WT, n = 9 KO), α-LP (n = 8 WT, n = 8 KO), ChILP (n = 6 WT, n = 6 KO), and ILCP (n = 8 WT, n = 8 KO). (e) Representative images of Peyer's patches (red arrows) in the small intestine from *Cxxc1*$^{f/f}$ *Rorc*^{Cre} mice and their wild-type *Cxxc1*$^{f/f}$ littermates. The numbers (f) and size (g) of Peyer's patches in the small intestine from *Cxxc1*$^{f/f}$ *Rorc*^{Cre} and *Cxxc1*$^{f/f}$ mice were compared (n = 10). Bar graphs are presented as mean ± SEM. A two-tailed Student's t-test was performed for comparisons. The data are representative of at least two independent experiments (a-g).

https://doi.org/10.1038/s43587-023-00453-7

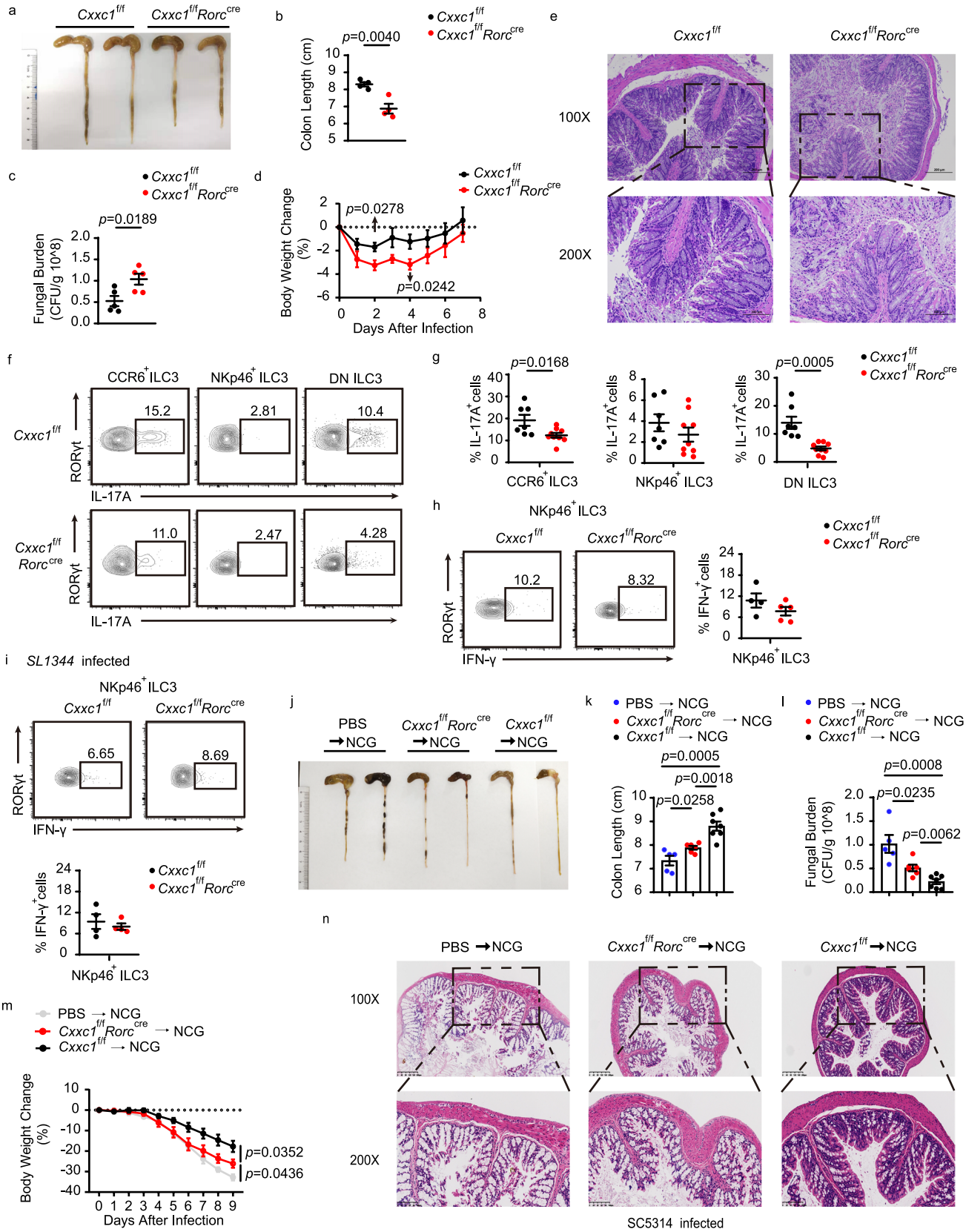

Extended Data Fig. 7 | See next page for caption.

https://doi.org/10.1038/s43587-023-00453-7

Extended Data Fig. 7 | Defective ILC3 function in Cxxc1-deficient mice compromises host defense against C. albicans infection. (a-g) *C. albicans* infection model. (a, b) Colon lengths of *Cxxc1*$^{f/f}$ and *Cxxc1*$^{f/f}$ *Rorc*^{Cre} mice (n = 4). (c) Fungal burden in faeces (n = 5). (d) Body weight changes (n = 5 WT, n = 8 KO). (e) H&E histological analysis of representative colons in infected mice. (f, g) Representative flow plots and quantification of IL-17A production by CCR6^{+} ILC3s (left), NKp46^{+} ILC3s (middle), and DN ILC3s (right) isolated from the siLP (n = 7 WT, n = 9 KO). (h-i) Cytokine production in siLP ILC3s from *Cxxc1*$^{f/f}$ and *Cxxc1*$^{f/f}$ *Rorc*^{Cre} mice. (h) Flow cytometric analysis of IFN-γ expression in NKp46^{+} ILC3s after stimulation with PMA and ionomycin (left); right, quantification (n = 4 WT, n = 5 KO). (i) *S. typhimurium* infection model. Representative flow cytometric profiles (left); right, quantification (n = 4). (j-n) *Cxxc1*$^{f/f}$ or *Cxxc1*$^{f/f}$ *Rorc*^{Cre} ILC3s (Lin^{-}CD127^{+}CD27^{-}KLRG1^{-}) were adoptively transferred into NCG mice with *C. albicans* infection. Measurements (j) and statistical analysis (k) of the colon lengths from NCG recipients (n = 5 control, n = 7 WT transferred, n = 6 KO transferred). (l) CFUs in the faeces of NCG recipients 9 days after infection (n = 5 control, n = 7 WT transferred, n = 6 KO transferred). (m) Changes in body weight were recorded at the indicated time points (n = 5 control, n = 7 WT transferred, n = 8 KO transferred). (n) Histological analysis of colonic tissues by H&E staining. Bar graphs are presented as mean ± SEM. A two-tailed Student's t-test was performed for comparisons. The data are representative of two independent experiments (a-g, i-n) and three independent experiments (h).

https://doi.org/10.1038/s43587-023-00453-7

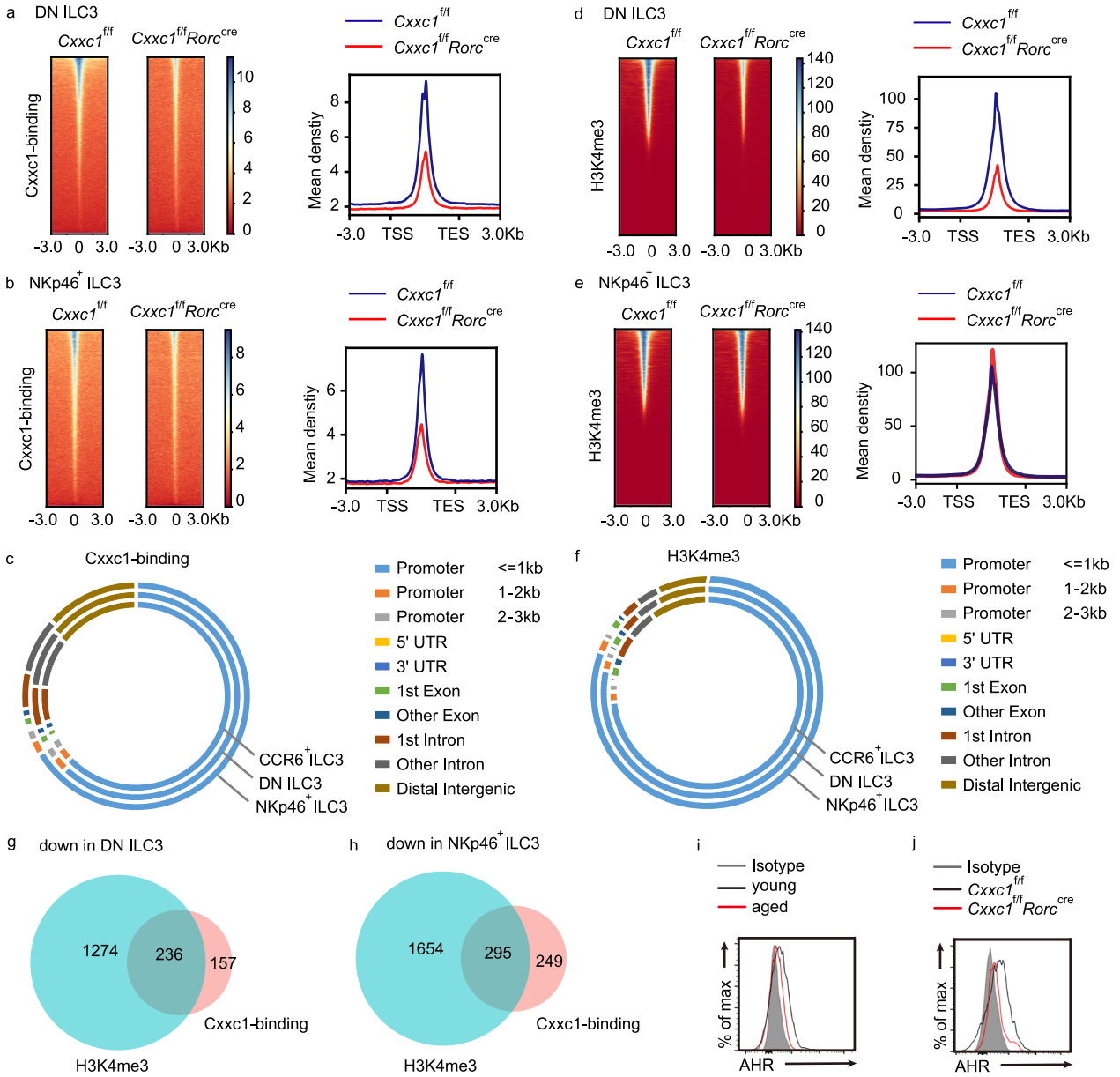

Extended Data Fig. 8 | The epigenetic program of DN ILC3s and NKp46+ ILC3s. (a, b) Heatmap for genome-wide distribution of Cxxc1-binding signals at peak centers in DN ILC3s (a) and NKp46$^+$ ILC3s (b) sorted from control and Cxxc1-deficient mice by CUT&Tag. (c) Donut chart showing the percentages of Cxxc1-binding at promoter regions, gene body regions, or intergenic regions. (d, e) Heatmaps illustrating enrichment of H3K4me3 CUT&Tag signals at all gene promoters (± 3 kb of TSS) in DN ILC3s (d) and NKp46$^+$ ILC3s (e). (f) Donut chart showing the percentages of H3K4me3 peaks at promoter regions, gene body regions, or intergenic regions. Peak annotation was performed by HOMER. UTR, untranslated region. (g, h) Venn diagram showing genes with reduced enrichment of Cxxc1 and H3K4me3 modification in the indicated cells in the graphs (Chi-squared test was used to calculate the P values. Adjusted absolute log2fc value > 0.25 and adjusted P value < 0.05). (i) Overlaid histograms show expression of indicated protein in aged mice (red), control mice (blue) and Isotype (grey). (j) Overlaid histograms show expression of indicated protein in *Cxxc1*$^{f/f}$*Rorc*^{Cre} mice (red), control mice (blue) and Isotype (grey). The data are representative of two independent experiments (i) and four independent experiments (j).

https://doi.org/10.1038/s43587-023-00453-7

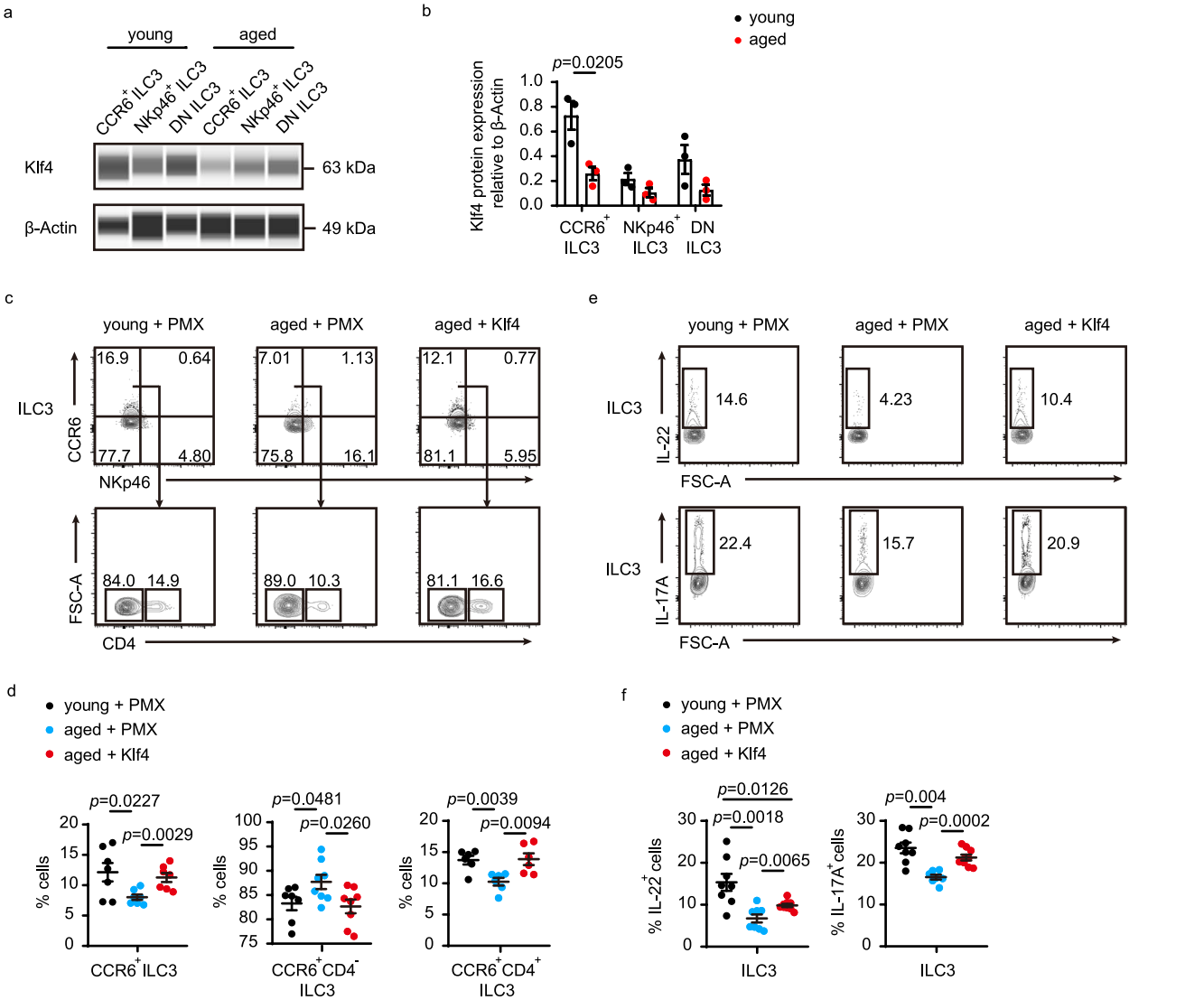

Extended Data Fig. 9 | Homeostasis and function of ILC3s in aged mice can be rescued by Klf4. (a) Immunoblot images showing Klf4 protein in ILC3 subsets sorted from the young and aged mice. (b) The relative protein content was normalized to β-Actin (n = 3). (c-f) Rescue experiments with ILC3s in aged mice. (c) Flow cytometry of CD45.2$^+$GFP$^+$ ILC3 subsets isolated from the siLP in mice that received retrovirus-transfected CLPs from the young and aged mice. ILC3 subsets are gated as CD45.2$^+$GFP$^+$Lin$^-$RORγt$^+$ and then CCR6$^+$NKp46$^-$, CCR6$^-$NKp46$^+$, or CCR6$^-$NKp46$^-$ (upper). The CD4$^+$ ILC3 subset among the CCR6$^+$ ILC3s was analyzed (below). (d) The percentages of the indicated subsets were compared (n = 6 or 7 young +PMX, n = 6,7 or 8 aged +PMX, n = 6,7 or 8 aged +Klf4). (e) Cytokine production in siLP CD45.2$^+$GFP$^+$ ILC3s from the indicated recipient mice. (f) The percentages of IL-22$^+$ ILC3s were compared (n = 8 young+PMX, n = 8 aged+PMX, n = 9 aged+Klf4). The percentages of IL-17A$^+$ ILC3s were compared (n = 8 young+PMX, n = 7 aged+PMX, n = 9 aged+ Klf4). Bar graphs are presented as mean ± SEM. A two-tailed Student's t-test was performed for comparisons. The data are representative of at least three independent experiments (a-f).

nature portfolio

Corresponding author(s): Chuan Wu, Han Liang, Lie Wang

Last updated by author(s): May 28, 2023

Reporting Summary

Nature Portfolio wishes to improve the reproducibility of the work that we publish. This form provides structure for consistency and transparency in reporting. For further information on Nature Portfolio policies, see our Editorial Policies and the Editorial Policy Checklist.

Statistics

For all statistical analyses, confirm that the following items are present in the figure legend, table legend, main text, or Methods section.

n/a	Confirmed
☐	☒ The exact sample size (*n*) for each experimental group/condition, given as a discrete number and unit of measurement
☐	☒ A statement on whether measurements were taken from distinct samples or whether the same sample was measured repeatedly
☐	☒ The statistical test(s) used AND whether they are one- or two-sided *Only common tests should be described solely by name; describe more complex techniques in the Methods section.*
☒	☐ A description of all covariates tested
☐	☒ A description of any assumptions or corrections, such as tests of normality and adjustment for multiple comparisons
☐	☒ A full description of the statistical parameters including central tendency (e.g. means) or other basic estimates (e.g. regression coefficient) AND variation (e.g. standard deviation) or associated estimates of uncertainty (e.g. confidence intervals)
☐	☒ For null hypothesis testing, the test statistic (e.g. *F*, *t*, *r*) with confidence intervals, effect sizes, degrees of freedom and *P* value noted *Give P values as exact values whenever suitable.*
☒	☐ For Bayesian analysis, information on the choice of priors and Markov chain Monte Carlo settings
☒	☐ For hierarchical and complex designs, identification of the appropriate level for tests and full reporting of outcomes
☒	☐ Estimates of effect sizes (e.g. Cohen's *d*, Pearson's *r*), indicating how they were calculated

Our web collection on statistics for biologists contains articles on many of the points above.

Software and code

Policy information about availability of computer code

Data collection	FACS Aria II flow cytometer, FlowJo'MIO software, Compass for Simple Western program (ProteinSimple),
Data analysis	Graph Pad Prism 8 was used for statistical analyses. Flow□□'"10 software was used for flow cytometer analysis CUT&Tag and analysis All raw sequence data were quality trimmed using fastp (version0.19.7) and aligned to the mm10 mouse genome using Bowtie2 (version 2.3.5.1) with options' –local–very-sensitive-local–no-unal–nomixed–no-discordant–phred33 -I 10 -X 700'. PCR duplicates were removed using Picard MarkDuplicates (version 2.25.0). Peaks were called using MACS2 (version 2.2.7.1) with options 'q 0.05'. DeepTools2 software (version 3.5.1) was used to create the peaks density plot and heatmap graph. Visualization of peak distribution along genomic regions of interested genes was performed with IGV. Genomic annotation was assigned using ChIPSeeker (version 1.28.3). Promoters were defined as follows: within 3000bp around the transcriptional start site (TSS). Differential expression analysis of two groups was performed using DESeq2 (version 1.30.1). scRNA-seq data analysis The fastq files were processed using the BD Rhapsody Targeted analysis pipeline on Seven Bridges. First, the read pair was removed if the mean base quality score is less than 20. Next, the filtered R1 reads were analyzed to identify the cell label sequences and unique molecular identifiers (UMIs). R2 reads were aligned to the mouse genome (mm10) using Bowtie2 (v 2.3.5.1) . Then, valid reads were collapsed into a single raw molecule based on the same cell label, UMI sequence and gene. Recursive substation error correction (RSEC) was applied to correct sequencing and PCR errors of raw UMI counts. The RSEC-adjusted molecule matrices were used for downstream analysis. For quality control, cells with >25% mitochondrial UMI counts or fewer than 200 genes detected were filtered out. We followed the Scanpy workflow for downstream analyses. Specifically, we 1) applied the log1pCP10K normalization to the raw counts; 2) selected highly variable genes; 3) regressed out the effects of the total count per cell and the percentage of mitochondrial gene count; 4) calculated the first 50 principal components; 5) applied Harmony to remove sample-level batch effects; 6) reduced the data dimension

through UMAP ; 7) clustered the single cells using an unsupervised graph-based clustering algorithm, Leiden; 8) identified cluster-specific marker genes using Student's t-test; and 9) annotated the clusters for their major cell type identities based on the expression patterns of literature-derived marker genes.

For manuscripts utilizing custom algorithms or software that are central to the research but not yet described in published literature, software must be made available to editors and reviewers. We strongly encourage code deposition in a community repository (e.g. GitHub). See the Nature Portfolio guidelines for submitting code & software for further information.

Data

Policy information about availability of data

All manuscripts must include a data availability statement. This statement should provide the following information, where applicable:

- Accession codes, unique identifiers, or web links for publicly available datasets
- A description of any restrictions on data availability
- For clinical datasets or third party data, please ensure that the statement adheres to our policy

This original data presented in the study can be found on GEO and available from the corresponding authors upon reasonable request. Single cell RNAseq (GSE208733, GSE210195, GSE210193, GSE209592) and CUT&Tag (GSE211017, GSE210194). Source data are provided with this paper.

Field-specific reporting

Please select the one below that is the best fit for your research. If you are not sure, read the appropriate sections before making your selection.

☒ Life sciences ☐ Behavioural & social sciences ☐ Ecological, evolutionary & environmental sciences

For a reference copy of the document with all sections, see nature.com/documents/nr-reporting-summary-flat.pdf

Life sciences study design

All studies must disclose on these points even when the disclosure is negative.

Sample size	No statistical methods were used to predetermine sample sizes, but our sample sizes are similar to those reported in previous publications(Gao X, Shen X, Liu K, et al. Front Immunol. 2022;13:939033. Published 2022 Jul 1.;Yin S, Yu J, Hu B, et al. Front Immunol. 2018;9:2101. Published 2018 Sep 12.). Data distribution was assumed to be normal, but this was not formally tested.
Data exclusions	No data points were excluded from analysis.
Replication	Experiments were performed independently for two to three times. And each experiment gave similar results.
Randomization	Mice of comparable age and body weight were randomly assigned to groups prior to the initiation of experiment.
Blinding	Data collection and analysis were not performed blind to the conditions of the experiments.

Reporting for specific materials, systems and methods

We require information from authors about some types of materials, experimental systems and methods used in many studies. Here, indicate whether each material, system or method listed is relevant to your study. If you are not sure if a list item applies to your research, read the appropriate section before selecting a response.

Materials & experimental systems

n/a	Involved in the study
☐	☒ Antibodies
☐	☒ Eukaryotic cell lines
☒	☐ Palaeontology and archaeology
☐	☒ Animals and other organisms
☒	☐ Human research participants
☒	☐ Clinical data
☒	☐ Dual use research of concern

Methods

n/a	Involved in the study
☐	☒ ChIP-seq
☐	☒ Flow cytometry
☒	☐ MRI-based neuroimaging

Antibodies

Antibodies used	The following antibodies were used: Antibody / Company / Dillution used / Catalogue number The following antibodies were used for flow cytometry:

CD27 PE-cy7 (clone LG.7F9) invitrogen 1:400 Cat# 25-0271-80
CD127 PE (clone A7R34) invitrogen 1:500 Cat# 12-1271-83
IL-22 APC (clone IL22JOP) invitrogen 1:500 Cat# 17-7222-82
CD4 APC-cy7 (clone RM4-5) invitrogen 1:500 Cat# 47-0042-82
CCR6 PE-cy7 (clone 29-2L17) Biolegend 1:200 Cat# 129816
PLZF PE (clone 9E12) Biolegend 1:400 Cat# 145803
NKp46 APC (clone 29A1.4) Biolegend 1:200 Cat# 137608
NKp46 FITC (clone 29A1.4) Biolegend 1:200 Cat# 137606
C-KIT APC-cy7 (clone 2B8) Biolegend 1:400 Cat# 105837
α4β7 APC (clone DATK32) Biolegend 1:400 Cat# 120607
Sca-1 PE (clone D7) Biolegend 1:200 Cat# 108107
CD45.1 PE (clone A20) Biolegend 1:500 Cat# 110708
KLRG1 PE-cy7 (clone 2F1) Biolegend 1:200 Cat# 138416
CD127 Bv421 (clone A7R34) Biolegend 1:200 Cat# 135024
CCR6 Bv421 (clone 29-2L17) Biolegend 1:200 Cat# 129817
CD25 Bv421 (clone PC61) Biolegend 1:400 Cat# 102034
Streptavidin Bv650 Biolegend 1:200 Cat# 405232
Fc block（clone 93）Biolegend 1:200 Cat# 101320
Flt3 PE-cy5 (clone A2F10) eBioscience 1:200 Cat# 15-1351-82
Isotype PE (clone P3.6.2.8.1) eBioscience 1:200 Cat# 12-4714-82
AHR PE (clone 4MEJJ) eBioscience 1:200 Cat# 12-5925-82
CD127 PE-cy7 (clone A7R34) eBioscience 1:200 Cat# 25-1271-82
IL-17A PE (clone TC11-18H10) BD Bioscience 1:200 Cat# 559502
IFN-γ PE (clone XMG1.2) BD Bioscience 1:200 Cat# 554412
CD45.2 APC (clone 104) BD Bioscience 1:200 Cat# 558702
RORγt PE (clone Q31-378) BD Bioscience 1:200 Cat# 562607
RORγt Bv421 (clone Q31-378) BD Bioscience 1:200 Cat# 562894
Streptavidin APC-cy7 BD Bioscience 1:200 Cat# 554063
CD45.2 Bv605 (clone 104) BD Bioscience 1:200 Cat# 563051
Fixable Viability Dye eFluor™ 520 eBioscience 1:200 Cat# 65-0867-14

Biotin：
CD3e（clone 145-2C11）invitrogen 1:400 Cat# 13-0031-85
TCRγδ（clone GL3?invitrogen 1:400 Cat# 13-5711-85
CD19（clone 1D3）invitrogen 1:400 Cat# 13-0193-85
Gr-1（clone RB6-8C5）Biolegend 1:400 Cat# 108404
TER-119（clone TER-119）Biolegend 1:400 Cat# 116204
CD5 （clone 53-7.3）Biolegend 1:500 Cat# 100604
B220（clone N418）Biolegend 1:400 Cat# 117303
NK1.1（clone PK136）Biolegend 1:500 Cat# 108704
CD11c（clone N418）Biolegend 1:500 Cat# 117303
CD11b（clone M1/70）Biolegend 1:400 Cat# 101204

The following antibodies were used for Wes：
Cxxc1（polyclonal）Abcam 1:100 Cat# ab56035
Klf4（polyclonal）invitrogen 1:100 Cat# PA5-23184
β-Actin (clone 13E5) CST 1:1000 Cat# 4970
Anti-Rabbit Secondary HRP Antibody ProteinSimple 1:5000 Cat# 042-206

The following antibodies were used for CUT&Tag：
Histone H3K4me3 antibody（polyclonal）Active Motif 1:50 Cat# 39016
Cxxc1（clone EPR19199）Abcam1:50 Cat# ab198977
Goat anti-Rabbit IgG (H+L)（polyclonal）Sigma-Aldrich 1:100 Cat# SAB3700883

Validation

The following antibodies were used: Antibody / Company / Dillution used / Catalogue number/ Validation

The following antibodies were used for flow cytometry:
CD27 PE-cy7 (clone LG.7F9) invitrogen 1:400 Cat# 25-0271-80 RRID: AB_1724037
CD127 PE (clone A7R34) invitrogen 1:500 Cat# 12-1271-83 RRID: AB_465845
IL-22 APC (clone IL22JOP) invitrogen 1:500 Cat# 17-7222-82 RRID: AB_10597583
CD4 APC-cy7 (clone RM4-5) invitrogen 1:500 Cat# 47-0042-82 RRID: AB_1272183
CCR6 PE-cy7 (clone 29-2L17) Biolegend 1:200 Cat# 129816 RRID: AB_2072798
PLZF PE (clone 9E12) Biolegend 1:400 Cat# 145803 RRID: AB_2561966
NKp46 APC (clone 29A1.4) Biolegend 1:200 Cat# 137608 RRID: AB_10612758
NKp46 FITC (clone 29A1.4) Biolegend 1:200 Cat# 137606 RRID: AB_2298210
C-KIT APC-cy7 (clone 2B8) Biolegend 1:400 Cat# 105837 RRID: AB_2616738
α4β7 APC (clone DATK32) Biolegend 1:400 Cat# 120607 RRID: AB_10719833
Sca-1 PE (clone D7) Biolegend 1:200 Cat# 108107 RRID: AB_313344
CD45.1 PE (clone A20) Biolegend 1:500 Cat# 110708 RRID: AB_313497
KLRG1 PE-cy7 (clone 2F1) Biolegend 1:200 Cat# 138416 RRID: AB_2561736
CD127 Bv421 (clone A7R34) Biolegend 1:200 Cat# 135024 RRID: AB_11218800
CCR6 Bv421 (clone 29-2L17) Biolegend 1:200 Cat# 129817 L RRID: AB_10898320
CD25 Bv421 (clone PC61) Biolegend 1:400 Cat# 102034 RRID: AB_11203373
Streptavidin Bv650 Biolegend 1:200 Cat# 405232 passed BioLegend's QC testing
Fc block（clone 93）Biolegend 1:200 Cat# 101320 RRID: AB_1574975

Flt3 PE-cy5 (clone A2F10) eBioscience 1:200 Cat# 15-1351-82 RRID: AB_494219
Isotype PE (clone P3.6.2.8.1) eBioscience 1:200 Cat# 12-4714-82 RRID: AB_470060
AHR PE (clone 4MEJJ) eBioscience 1:200 Cat# 12-5925-82 RRID: AB_2572644
CD127 PE-cy7 (clone A7R34) eBioscience 1:200 Cat# 25-1271-82 RRID: AB_469649
IL-17A PE (clone TC11-18H10) BD Bioscience 1:200 Cat# 559502 RRID: AB_397256
IFN-γ PE (clone XMG1.2) BD Bioscience 1:200 Cat# 554412 RRID: AB_395376
CD45.2 APC (clone 104) BD Bioscience 1:200 Cat# 558702 RRID: AB_1645215
RORγt PE (clone Q31-378) BD Bioscience 1:200 Cat# 562607 RRID: AB_11153137
RORγt Bv421 (clone Q31-378) BD Bioscience 1:200 Cat# 562894 RRID: AB_2687545
Streptavidin APC-cy7 BD Bioscience 1:200 Cat# 554063 RRID: AB_10054651
CD45.2 Bv605 (clone 104) BD Bioscience 1:200 Cat# 563051 RRID: AB_2737974

Biotin
CD3e clone 145-2C11 invitrogen 1:400 Cat# 13-0031-85 RRID: AB 466320
TCRγδ clone GL3?invitrogen 1:400 Cat# 13-5711-85 RRID: AB_466669
CD19 clone 1D3 invitrogen 1:400 Cat# 13-0193-85 RRID: AB_657658
Gr-1 clone RB6-8C5 Biolegend 1:400 Cat# 108404 RRID: AB_313369
TER-119 clone TER-119 Biolegend 1:400 Cat# 116204 RRID: AB_313705
CD5 clone 53-7.3 Biolegend 1:500 Cat# 100604 RRID: AB_312733
B220 clone N418 Biolegend 1:400 Cat# 117303 RRID: AB_313772
NK1.1 clone PK136 Biolegend 1:500 Cat# 108704 RRID: AB_313391
CD11c clone N418 Biolegend 1:500 Cat# 117303 RRID: AB_313772
CD11b clone M1/70 Biolegend 1:400 Cat# 101204 RRID: AB_312787

Eukaryotic cell lines

Policy information about cell lines

Cell line source(s)	Plat E cell line was purchased from Cell Bank, China.
Authentication	The Platinum-E (Plat-E) Cell Line, a potent retrovirus packaging cell line based on the 293T cell line, was generated using novel packaging constructs with an EF1α promoter to ensure longer stability and highyield retroviral structure protein expression (gag, pol, ecotropic env). Plat-E cells can be kept in good condition for at least 4 months in the presence of drug selection, and can produce retroviruses with an average titer of 1 x 107 infectious units/mL by transient transfection. In addition, replication competent retroviruses (RCR) are virtually nonexistent because only coding sequences of viral structural genes are used, avoiding any unnecessary retroviral sequences. The Plat-E cell line is designed for rapid, transient production of high-titer ecotropic retrovirus
Mycoplasma contamination	All cell lines tested negative for mycoplasma.
Commonly misidentified lines (See ICLAC register)	No commonly misidentified cell lines were used in this study.

Animals and other organisms

Policy information about studies involving animals; ARRIVE guidelines recommended for reporting animal research

Laboratory animals	The Cxxc1f/f mouse strain has been described before33. The Rorc-cre mice (JAX: 022791) were kindly provided by Prof. Ju Qiu (Shanghai Institutes for Biological Sciences, Chinese Academy of Sciences). Cxxc1f/f mice were crossed to Rorc-cre mice to generate respective conditional knockout mice. NOD Prkdcem26Cd52Il2rgem26Cd22/Nju (NCG, T001475) mice were purchased from Nanjing Biomedical Research Institute of Nanjing University. Mice were used at 6-8 weeks of age and kept co-housed after weaning. Young (6- to 8-week-old) and aged (18-month-old) mice of C57BL/6J background were obtained from Zhejiang University Laboratory Animal Center, as well as CD45.1 mice (2-month-old). All mice were bred and maintained under specific pathogen-free conditions at the Zhejiang University Laboratory Animal Center, and all procedures involving animals were approved by the Zhejiang University Animal Care and Use Committee; approval no. ZJU20230177. The mice had free access to clean water and food. Animals were assigned experimental groups at random. Mice at 6–8 weeks of age were used for all experiments otherwise noted. The numbers and gender of mice per experimental group are indicated in the figure legends. All experiments were performed in accordance with the guidelines from the Animal Research and Ethics Boards of Zhejiang University.
Wild animals	No wild animals were used in this study.
Field-collected samples	This study did not use samples collected from the field.
Ethics oversight	All procedures involving animals were approved by the Zhejiang University Animal Care and Use Committee; approval no. ZJU20230177. All experiments were performed in accordance with the guidelines from the Animal Research and Ethics Boards of Zhejiang University.

Note that full information on the approval of the study protocol must also be provided in the manuscript.

ChIP-seq

Data deposition

☒ Confirm that both raw and final processed data have been deposited in a public database such as GEO.

☒ Confirm that you have deposited or provided access to graph files (e.g. BED files) for the called peaks.

Data access links *May remain private before publication.*	https://www.ncbi.nlm.nih.gov/geo/query/acc.cgi?acc=GSE208733 https://www.ncbi.nlm.nih.gov/geo/query/acc.cgi?acc=GSE210195 https://www.ncbi.nlm.nih.gov/geo/query/acc.cgi?acc=GSE210193 https://www.ncbi.nlm.nih.gov/geo/query/acc.cgi?acc=GSE209592 https://www.ncbi.nlm.nih.gov/geo/query/acc.cgi?acc=GSE211017 https://www.ncbi.nlm.nih.gov/geo/query/acc.cgi?acc=GSE210194
Files in database submission	Including clean data and processed data.
Genome browser session (e.g. UCSC)	https://genome.ucsc.edu/cgi-bin/hgTracks?db=mm10&lastVirtModeType=default&lastVirtModeExtraState=&virtModeType=default&virtMode=0&nonVirtPosition=&position=chr12%3A56694976%2D56714605&hgsid=1412968251_UXzUgkz6Qf0H8xDxbNxf9jPNdTBU

Methodology

Replicates	All chip-seq data included at least two biological replicates, and each replicate was derived from three mice of the same sex and cage.
Sequencing depth	Long & paired-end reads. clean reads:10304570. Unique mapping rate 73.65% ~ 84.04%.
Antibodies	H3K4me3 antibody (39016, Active Motif), Cxxc1 antibody (ab198977, Abcam,provided by Prof. Hengyu Fan Institute of Life Sciences, Zhejiang University) was added and incubated overnight at 4°C with slow rotation. secondary antibody (Goat anti-Rabbit IgG, SAB3700883; Sigma-Aldrich)
Peak calling parameters	Peaks were called using MACS2 (version 2.2.7.1) with options 'q 0.05'.
Data quality	All raw sequence data were quality trimmed using fastp (version0.19.7) and aligned to the mm10 mouse genome using Bowtie2 (version 2.3.5.1) with options' –local–very-sensitive-local–no-unal–nomixed–no-discordant–phred33 -I 10 -X 700'. PCR duplicates were removed using Picard MarkDuplicates (version 2.25.0). Peaks were called using MACS2 (version 2.2.7.1) with options 'q 0.05'. DeepTools2 software (version 3.5.1) was used to create the peaks density plot and heatmap graph. Visualization of peak distribution along genomic regions of interested genes was performed with IGV. Genomic annotation was assigned using ChIPSeeker (version 1.28.3). Promoters were defined as follows: within 3000bp around the transcriptional start site (TSS). Differential expression analysis of two groups was performed using DESeq2 (version 1.30.1).
Software	fastp (version0.19.7) , Bowtie2 (version 2.3.5.1) , Picard MarkDuplicates (version 2.25.0), MACS2 (version 2.2.7.1) , DeepTools2 software (version 3.5.1) , ChIPSeeker (version 1.28.3), DESeq2 (version 1.30.1).

Flow Cytometry

Plots

Confirm that:

☒ The axis labels state the marker and fluorochrome used (e.g. CD4-FITC).

☒ The axis scales are clearly visible. Include numbers along axes only for bottom left plot of group (a 'group' is an analysis of identical markers).

☒ All plots are contour plots with outliers or pseudocolor plots.

☒ A numerical value for number of cells or percentage (with statistics) is provided.

Methodology

Sample preparation	After euthanizing the mouse, the small intestine was removed. Briefly, small intestines were dissected, and fat tissues and Peyer's patches were removed. Intestines were dissected longitudinally and subsequently cut into 5mm-long pieces, followed by washing with DMEM. The intestinal pieces were then incubated in DMEM containing 3% fetal bovine serum (FBS), 0.2% Hanks, 0.5 M EDTA, and dithiothreitol (0.145 mg/ml) for 10 min with constant agitation by droppers. The tissues were then digested with DNase I (Sigma; 50 mg/ml) and collagenase II (Worthington-Biochem; 145 mg/ml) in DMEM at 37°C for 5 min. The dissociated cells were filtered with a 100 µm cell strainer and harvested from the interphase of an 80% and 40% Percoll (GE Healthcare) gradient. After being washed with PBS and resuspended, LPLs were collected for further analysis.
Instrument	FACS Aria II flow cytometer
Software	Data collection: BDFACSDiva (v8.0.1) software Data analysis: FFlowJo™10 software

Cell population abundance	Cell populations were sorted at >95% purity, determined by flow cytometric analysis of post-sort samples.
Gating strategy	Gating strategy is exemplified in the extended data figures and was reported in our previous publication (Gao X, Shen X, Liu K, et al. Front Immunol. 2022;13:939033. Published 2022 Jul 1.;Yin S, Yu J, Hu B, et al. Front Immunol. 2018;9:2101. Published 2018 Sep 12.). Briefly, all cell events on FSC/SSC plot are included as the starting cell population, followed by excluding debris, dead cells and non-immune cells based on differential staining of viability dye. Doublets are excluded based on SSC-A/SSC-H plot. Live leukocyte singlets are used to define immune cell subsets based on characteristic surface markers. For each marker, "positive" and "negative" cell populations are defined based on FMO. CCR6+ ILC3s (Lin-CD127+CD27-KLRG1-CCR6+NKp46-)、NKp46+ ILC3s (Lin-CD127+CD27-KLRG1-CCR6-NKp46+) and DN ILC3s (Lin-CD127+CD27-KLRG1-CCR6-NKp46-). CLPs (Lin-CD127+c-KitintSca-1intFlt3+).

☒ Tick this box to confirm that a figure exemplifying the gating strategy is provided in the Supplementary Information.